

Raport științific

privind implementarea proiectului 269/5.10.2011, cod CNCSIS PN-II-ID-PCE-2011-3-0650, în perioada ianuarie – octombrie 2013

Titlu: Studiul interacțiunii polimer-radiație laser în atmosfera controlată. Obținerea de filme nanostructurate prin ablație laser. Aplicații

Obiective generale:

- Studiul plasmei de ablație laser în regim nanosecundă și femtosecundă
- Studiul dinamicii plasmei de ablație laser folosind ținte metalice

Pentru îndeplinirea acestor obiective au fost parcurse următoarele activități :

- A. S-a studiat influența lărgimii pulsului laser asupra plasmei de ablație laser ;
- B. S-au folosit tehnici spectrale specifice plasmei tranzitorii și de imaginerie ultrarapidă ICCD pentru caracterizarea și rezolvarea spatio-temporală a plumei de ablație laser ;
- C. Au fost studiate oscilațiile electrice care apar în circuitele electronice ale unor electrozi plasați în vecinătatea plumei de ablație laser (ținte, pèreți, sonde, etc) sub incidența plumei de ablație laser ;
- D. Au fost analizate influența diferitelor materiale (tip țintă) asupra dinamicii plamei de ablație laser. Rezultatele au fost comparate cu cele obținute în studiul plasmei staționare asupra unor formațiuni de plasmă neomogene cu structură de potențial nemonotonă. Aceste structuri au fost identificate ca fiind straturi duble respectiv straturi multiple de plasmă, funcție de condițiile experimentale.

În cadrul acestor cercetări au fost dezvoltate tehnici, metode de caracterizare și obținere a unor materiale de interes tehnologic iar rezultatele obținute au fost publicate în reviste cotate ISI și în cadrul unor conferințe naționale sau internaționale ca lucrări orale, postere sau invitate după cum urmează:

Lucrări ISI

1. G. Dascalu, G. Pompilian, B. Chazallon, O. F. Caltun, S. Gurlui, C. Focsa, *Femtosecond pulsed laser deposition of cobalt ferrite thin films*, Applied Surface Science, Volume 278, p. 38-42 (2013)
2. S. Gurlui, G. O. Pompilian, P. Nemec, V. Nazabal, M. Ziskind, C. Focsa, *Plasma Diagnostics in Pulsed Laser Deposition of GaLaS Chalcogenides*, Appl. Surf. Science, 278, p. 352-356 (2013)
3. G. Dimitriu, M. Aflori, L. M. Ivan, V. Radu, E. Poll, M. Agop, *Experimental and theoretical investigations of plasma multiple double layers and their evolution to chaos*, Plasma Sources Sci. Technology, 22, 035007 (2013) doi:10.1088/0963-0252/22/3/035007

Lucrări invitate

1. S. Gurlui, P. Nica, M. Agop, M. Osiac, C. Focsa, Peculiar Behavior of Plasma Plumes Generated by Femtosecond Laser Ablation of Metallic Targets, 12th International Conference on Laser Ablation, 6-11 October 2013, Ischia, Italy (O-09).
2. S. Gurlui, P. Nica, M. Agop, M. Osiac, C. Focsa, Two-Temperature Plasmas Generated by Femtosecond Laser Ablation of Metallic Targets, 16th International Conference On Plasma Physics And Applications, June 20-25, 2013, Magurele, Bucharest, ROMANIA
3. C. Focsa, S. Gurlui, High Technological, Potential Materials, Explored by Laser, Ablation, The 5-th National Conference of Applied Physics, MAY 23 - 24, 2013, Iasi, Romania

Conferințe naționale și internaționale

1. O. G. Pompilian, G. Dascalu, I. Mihaila, S. Gurlui, M. Olivier, P. Nemeș, V. Nazabal, N. Cimpoeșu, C. Focsa, Pulsed Laser Deposition of Gallium Lanthanum Sulphide Chalcogenide Thin Films, 12th International Conference on Laser Ablation, 6-11 October 2013, Ischia, Italy (P2-69);
2. O. Niculescu, M. M. Cazacu, M. N. Dănilă, D. G. Dimitriu, S. Gurlui, M. Agop – Magnetosphere double layers and aurora borealis. Acceleration mechanisms and instabilities, *Environmental Legislation, Safety Engineering and Disaster Management (ELSEEDIMA)*, Cluj-Napoca, Romania, 2012;
3. S. Gurlui, O. Niculescu, D. G. Dimitriu, C. Ionita, R. Schrittwieser – Spectral investigations of two simultaneous fireballs in plasma, *Physics Conference TIM-12*, Timisoara, Romania, 2012;
4. O. Niculescu, S. Gurlui, D. G. Dimitriu, C. Ionita, R. Schrittwieser – Optical Emission Spectroscopy and Nonlinear Dynamics Analysis of Two Fireballs Simultaneously Obtained in a Cold Diffusion Plasma, *31st ICPIG*, July 14-19, Granada, Spain, 2013;
5. O. Niculescu, S. Gurlui, D. G. Dimitriu, C. Ionita, R. Schrittwieser – Study on the Interaction of two Complex Plasma Structures. Optical Emission Spectroscopy and Nonlinear Dynamics Analysis, *PLASMA-2013*, September 2-6, Warsaw, Poland, 2013.

Anexam revistele ISI publicate.

Toate obiectivele propuse au fost indeplinite

12 octombrie 2013

Director de proiect,
Conf. Dr Silviu GURLUI





Plasma diagnostics in pulsed laser deposition of GaLaS chalcogenides

O.G. Pompilian^a, S. Gurlui^{b,*}, P. Nemeč^c, V. Nazabal^d, M. Ziskind^a, C. Focsa^a

^a Laboratoire de Physique des Lasers, Atomes et Molécules (UMR 8523), Université Lille 1, 59655 Villeneuve d'Ascq cedex, France

^b Physics Department, Alexandru Ioan Cuza University of Iasi, 700506 Iasi, Romania

^c Faculty of Chemical Technology, University of Pardubice, Studentska 573, 53210 Pardubice, Czech Republic

^d Laboratoire des Verres et Céramiques, Université de Rennes 1, Campus de Beaulieu, 35042 Rennes cedex, France

ARTICLE INFO

Article history:

Available online 23 November 2012

Keywords:

Pulsed laser deposition

Plasma dynamics

Optical emission spectroscopy

Chalcogenides

ABSTRACT

The aim of this work is to characterize the ejection plume obtained by laser ablation of GaLaS (GLS) samples in order to better understand the ablation phenomena for optimizing the pulsed laser deposition of chalcogenide thin films. The dynamics of the plasma between target and substrate was investigated through time- and space-resolved optical emission spectroscopy. High-resolution optical spectra have been recorded in the UV–VIS range using a 500-mm focal length monochromator and a fast gate ICCD camera. From the space–time evolution of the optical signals, the velocities of various species (including neutrals and ions) have been derived. Using the relative intensity method, the space- and time-evolution of the excitation temperature and electronic density have been determined. A complex behavior of the laser ablation plasma has been revealed.

© 2012 Elsevier B.V. All rights reserved.

1. Introduction

Amorphous chalcogenides represent an important segment of IR-transparent materials with multiple applications in, e.g. the development of amplifiers and laser sources, optical sensors and all-optical processing components based on non-linear properties [1–5]. In this frame, a special chalcogenide glasses class, namely gallium lanthanum sulphide (GLS), has been evidenced (in particular when doped with rare earth elements) as an attractive non-toxic alternative to arsenic-based glasses, with optical transparency from the visible to infrared wavelengths, thermal stability, high refractive indices, high rare-earth solubility, high transition temperature and large photoinduced effects [6–9]. These glasses are stable, hard, and non-hygroscopic and can be involved in a wide range of novel opto-electronic applications based on their photo-stimulated properties (absorption edge shifts, photo-induced refractive index changes, photo-sensitivity, etc.) [10–12].

For some of the applications listed above (especially those related to integrated optics), the processing of the chalcogenide glasses in form of thin films is necessary. Numerous methods of preparation are available (spin coating, thermal evaporation in vacuum, ionic and magnetron sputtering, CVD, etc.), yet synthesis of chalcogenide thin films of complex composition, desired stoichiometry, good homogeneity and adhesion to the substrate and

other specific physico-chemical properties is often found to be a difficult task for these “classical” methods. Pulsed laser deposition (PLD) evolved as one of the prospective techniques in this field, due to the simplicity of its principle, the possibility to obtain stoichiometric transfer of target material to the substrate and to fabricate films of unusual composition [3]. Although the PLD technique has been employed for almost two decades [13] to grow chalcogenide thin films, the control and optimization of the deposition parameters are still generally done in an empirical manner. For the detailed understanding of the processes connected with PLD and particularly for the optimization of the PLD of amorphous chalcogenide films, studying the dynamics of the plasma plume formed during laser ablation is appealing. Despite the numerous works available in the literature on the PLD growth of amorphous chalcogenides and related materials, only few of them tackled this issue using optical and electrical investigation methods [14,15]. Some authors characterized the composition of the ablation plume in terms of atoms, molecules or clusters by using time-of-flight mass spectrometry [16,17].

The aim of this work is therefore to investigate the dynamics of plasma plume generated by nanosecond laser ablation of GLS chalcogenide under vacuum. The behavior of the GLS plasma formation was investigated through time- and space-resolved high-resolution optical emission spectroscopy (OES) and fast gate ICCD imaging. From the space–time evolution of the optical signals, the velocities of various species present in the plasma (including neutrals and ions) along with temporal and spatial evolution of associated excitation temperatures and electronic densities have been derived.

* Corresponding author.

E-mail address: sgurlui@uaic.ro (S. Gurlui).

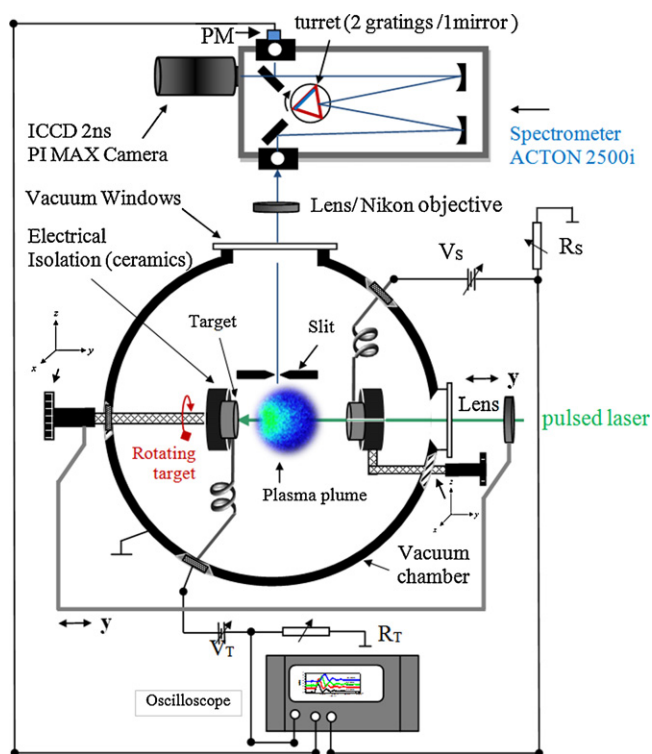


Fig. 1. Schematic view of the experimental set-up.

2. Experimental details

The experimental set-up employed for these measurements has been described previously [18–21]. A schematic view is presented in Fig. 1. The GLS chalcogenide target (20 mm diameter, 5 mm thick disk) is placed on a micrometric precision multi-axis translation–rotation stage in a $\sim 10^1$ vacuum chamber evacuated to a base pressure of 1×10^{-6} Torr by a 550 l/s turbomolecular pump (Agilent Technologies TV-551) coupled to a 12.6 m³/h dry fore pump (Agilent Technologies TS-300). The second harmonic ($\lambda = 532$ nm) of a 10 ns Nd:YAG pulsed laser beam (Continuum Surelite III-10) is focused (at normal incidence) by a $f = 25$ cm lens onto the GLS target, through a 1 mm diameter hole manufactured in the substrate holder used for thin film deposition. The estimated spot diameter at the impact point has been $\sim 700 \mu\text{m}$ for a laser energy of 15 mJ/pulse, leading to a fluence of $\sim 4 \text{ J/cm}^2$. The laser ablation plasma emission was visible to the naked-eye on a distance of ~ 1 cm along the normal to the target, expanding on several mm on the transversal direction. The formation and dynamics of the plasma plume have been studied by means of a high-resolution monochromator (Acton SP2500i, 500 mm focal length) and an intensified CCD camera (Roper Scientific PIMAX2-1003-UNIGEN2, 1024 \times 1024 pixels, minimum gating time 2 ns). The monochromator is fitted with one mirror and two diffraction gratings (3001/mm, blaze at 300 nm, and 24001/mm, blaze at 240 nm) mounted on the same three-position turret, which allows an easy switching between imaging, low-resolution, and high-resolution spectroscopy experiments. For the imaging experiments, a Nikon objective was used to form the image of the whole plasma plume on the ICCD array through the kinematic entrance slit (12 mm \times 12 mm opening) of the spectrometer and with the turret fixed in the mirror position. The ICCD camera was triggered on the TTL Q-switch output of the ablation laser (10 Hz repetition rate), and an internal routine was used to increment the delay between the laser pulse and the gate opening. For this configuration, gate widths of 5 ns were usually employed, in order to catch as much as

possible sharp temporal snapshots in the space–time evolution of the plume. Averaging on 20 snapshots for each delay has been performed. For spectrally resolved studies, the plasma plume emission was focused on the monochromator entrance slit by a $f = 40$ mm cylindrical lens (see Fig. 1). Low-resolution spectra were recorded using the 3001/mm grating and a monochromator entrance slit width of $50 \mu\text{m}$ in order to identify the spectral regions of interest. In this configuration, ~ 80 nm broad spectra were recorded for a given position of the grating, with a spectral resolution of ~ 0.5 nm. Finally, the high-resolution spectra were recorded with the 24001/mm grating and a slit width of $50 \mu\text{m}$, resulting in a spectral resolution of ~ 0.06 nm on ~ 8 nm broad spectra for a given grating position. The complete spectrum was obtained by using the “step-and-glue” procedure of the monochromator/camera software, which automatically increments the grating position once a given (80 nm or 8 nm wide) spectrum was recorded.

For space-resolved optical emission spectroscopy studies, a 1 mm \times 5 mm slit was placed in the vacuum chamber, at 40 mm from the normal to the target (see Fig. 1). This slit defined 1 mm width plasma plume “slices” parallel to the target surface, which were further imaged ($\sim 1:10$ magnification) by the cylindrical lens on the monochromator entrance slit. The slit was maintained fixed and, for spatial scanning, we translated the target and the laser focusing lens as a whole (i.e. without modifying the distance between them), as they were both attached to the same XYZ micrometric translation stage. This arrangement ensures the same ablation spot diameter on the target, i.e. the same fluence, for all the experiments performed. With this system, good spatial resolution (0.2 mm along the normal to the target, for a monochromator entrance slit of $20 \mu\text{m}$) and S/N ratio (usually >100) have been achieved.

The experimental set-up includes also electrical probes (target potential, Langmuir probes) linked to a fast digitizing oscilloscope (2 GHz, LeCroy) for transient plasma sub-ns investigations which are not presented in this paper.

3. Results and discussion

In order to obtain a preliminary insight on the dynamics of the laser GLS ablation plasma plume, ICCD sequential snapshots of the spectrally unresolved plasma optical emission are recorded at various delays (100–1300 ns) with respect to the laser pulse (Fig. 2). These pictures reveal the formation of a single plasma structure, on the contrary of some previous studies showing a splitting of the plume in two components (fast and slow) [14,15,20,21]. The average axial velocity of the maximum emitting point derived from these images (4.4×10^3 m/s) is of the same order of magnitude as

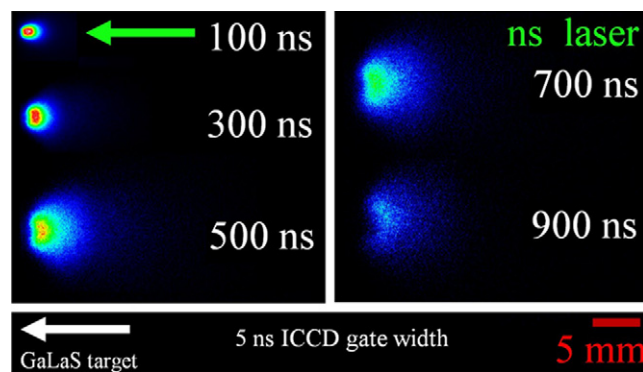


Fig. 2. Temporal evolution of the spectrally integrated optical emission of the plasma plume obtained by laser ablation of the GLS sample. Successive laser pulses of equal energy (15 mJ, fluence = 4 J/cm^2) were used to record the snapshots at different delays.

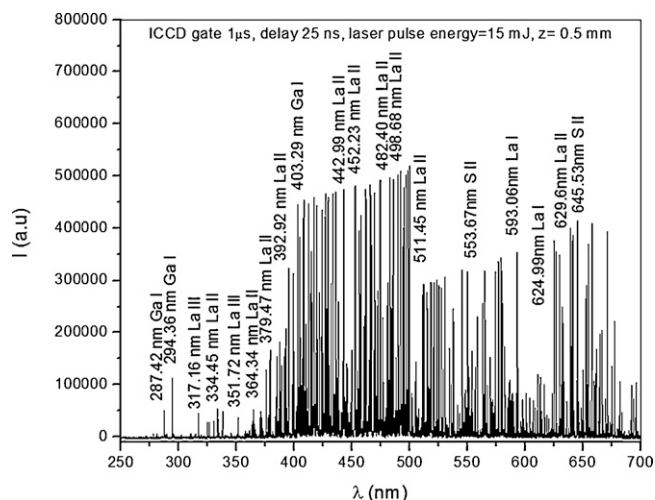


Fig. 3. Optical emission spectrum of a 0.2-mm-wide plasma slice centered at $z=0.5$ mm from the target surface (gate width = $1 \mu\text{s}$, delay = 25 ns, laser fluence = 4 J/cm^2).

in the “slow” component of plasma plume recorded for the AsSe system [14] and is lower than the value derived from time-of-flight Langmuir probe experiments on the nanosecond ablation of gadolinium gallium garnet [15]. We emphasize however that this velocity reflects only the evolution of the maximum emitting point in the plasma (which is ruled mainly by excitation collisions and radiative de-excitations), yet individual species with significantly higher velocities can be present in the plume. In order to separate the contribution of each species present in the plasma plume, we have performed a space- and time-resolved optical emission spectroscopy study using the technique described in [21]. Fig. 3 displays an overview of the 250–700 nm spectral range recorded in the vicinity of the target and the assignment of the most intense spectral observed lines. One can easily notice the presence of both neutral and ionic species in the spectrum, and even some signals from double-charged ions in the case of La. By using the scanning capabilities of the ICCD camera, temporal profiles of the emission lines at a given distance from the target can be recorded in seconds, as illustrated in Fig. 4. By recording these profiles at various distances from the target (z), and plotting the distance vs. the time needed to reach maximum emission, one can derive axial velocities for the individual species of interest. An example is given in Fig. 5 for the results obtained in the case of five neutral and singly charged

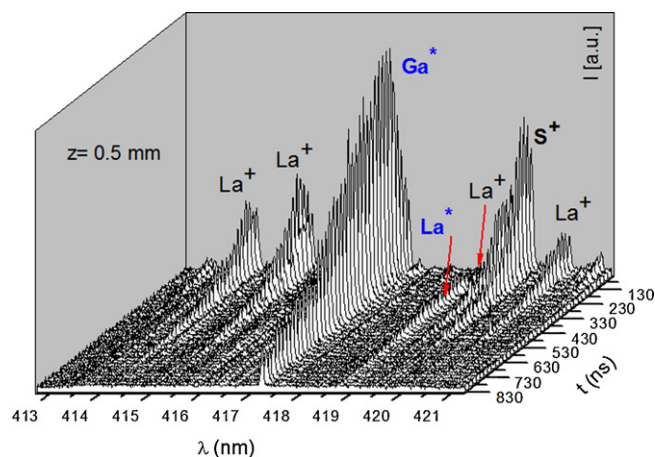


Fig. 4. Optical emission time-of-flight profiles recorded for various neutrals and ions spectral lines at $z=0.5$ mm from the target surface (gate width = 50 ns, laser fluence = 4 J/cm^2).

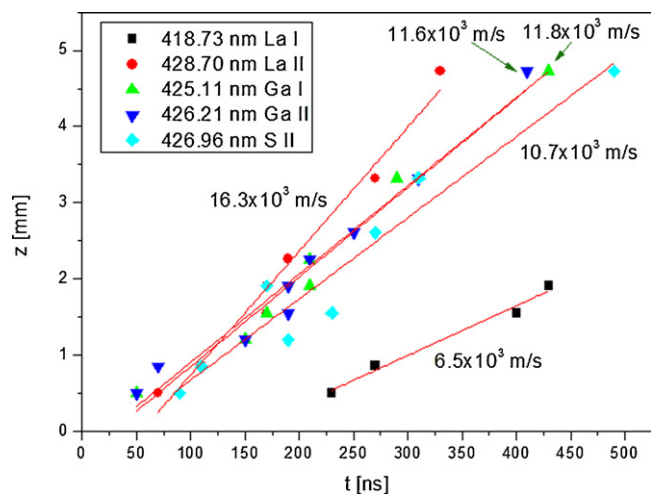


Fig. 5. Axial velocities of various Ga, La, and S species derived from the space–time evolution of spectral lines (gate width = 50 ns, laser fluence = 4 J/cm^2).

species of Ga, La, and S. The velocity values derived for these species and others (not displayed) are summarized in Table 1. These data show the presence of high kinetic energy species in the plume, with velocities in the range of 10^4 m/s. This is of practical importance for PLD, as energetic particles hitting the surface of a growing film can influence the nucleation, energy and mobility of adatoms on the surface of the film, by colliding with atoms already adhered to the existing islands, causing bond breaking or even sputtering. The velocity values displayed in Table 1 turn into kinetic energies ranging from 19 eV for S^+ to 190 eV for La^+ . It has been shown that for such high kinetic energies, sputtering rates exceeding 0.5 can be reached (Ag atoms, 4.5 J/cm^2 [22]). A possible solution is of course to reduce the fluence, but in this case stoichiometric transfer issues may arise [23].

Generally the expansion velocities of the ionized species are found to be higher than those of the excited neutral species [14,15,21]. This trend seems to be generally followed in our experiments (see Fig. 5), however some neutrals (e.g. Ga, see Table 1) can exhibit velocities comparable to those of the corresponding ions. This can be an evidence of a different ionization/excitation mechanism for this species, possibly resulting from in-plume collisional/radiative processes rather than directly from the ablation step.

In order to get some insight on the internal energies of the species present in the plume, the excitation temperature can be calculated using the relative intensities of two or more spectral lines originating from the same ionization stage, based on the well-known Boltzmann plot method [20,21]. An example is given in Fig. 6 for La II (spectroscopic constants from [24] have been used). Excitation temperatures for other species, recorded at $z=0.5$ mm from the target, are summarized in Table 1. Note that these are somehow

Table 1

Axial velocities and average excitation temperatures (at 0.5 mm from the target, $1 \mu\text{s}$ gate width, laser fluence = 4 J/cm^2) of some species present in the plasma plume.

Species	Velocity [10^3 m/s]	Excitation temperatures [10^3 K]
Ga I ($\lambda = 417.20$ nm)	9.9	4.3
Ga I ($\lambda = 425.11$ nm)	11.8	4.3
Ga II ($\lambda = 426.21$ nm)	11.6	
La I ($\lambda = 418.73$ nm)	6.5	5.3
La I ($\lambda = 428.02$ nm)	9.7	5.3
La I ($\lambda = 514.54$ nm)	11.2	5.3
La II ($\lambda = 428.70$ nm)	16.3	7.4
S II ($\lambda = 426.96$ nm)	10.7	1.4

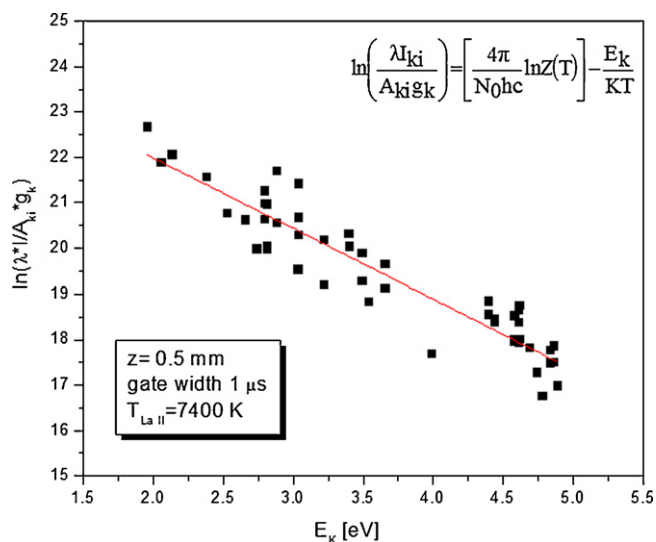


Fig. 6. Boltzmann plot for calculation of the average excitation temperature (gate width = 1 μ s) of La II at $z=0.5$ mm from the target surface (laser fluence = 4 J/cm²).

“averaged” temperatures, as the gate width of the detector was set to 1 μ s. Although the temperature values are rather common for this range of laser fluences, one can easily remark the very low temperature of S II, which can also indicate a different excitation mechanism for this species (note also that neutral sulfur emission lines have not been present in the spectrum).

Deeper insight on the plasma plume dynamics can be granted by studying the space- and time-resolved profiles of the excitation temperature and electronic density. For temporal temperature profiles, this can be done by series of snapshots taken at a given distance and various delays with respect to the laser pulse (as those in Fig. 4), calculating for each delay the ratio of two spectral lines intensities (this method was preferred here for simplicity and time-saving, instead of the “heavier” Boltzmann plot method used above to derive the “average” temperatures). Two examples are given in Fig. 7a and b for the temporal evolution of La⁺ (derived from the relative intensity of the 428.69 nm and 429.60 nm lines) at two distances from the target ($z=0.5$ mm and 1.55 mm, respectively). The temporally resolved (50 ns resolution) excitation temperatures obtained (roughly between 6500 K and 9500 K) are consistent with the average value (1 μ s) found at $z=0.5$ mm.

Moreover, the temporal evolution of the electronic density n_e can be calculated from the temperature temporal profile by using the relative intensities of the neutral atomic lines and singly charged ionic lines according to the Saha-Eggert equation [25,26]. Using the 428.026 nm and 428.696 nm spectral lines of La* and La⁺, respectively, and the spectroscopic data from [24], we derived the temporal profiles of the electron density displayed in Fig. 7. The electron density and temperature values (at least up to the onset of the oscillations) seem to be in fair agreement with previous studies performed at comparable fluences, but on completely different materials (Ag [27] and Cu [28]). This somehow suggests a quite universal behavior in this range of fluence, which can be related [23] to the not so different cohesive energies (vaporization enthalpies) of e.g. Ag, Cu, Ga and La (at least in pure solid samples). Note however that S is much more volatile (by two orders of magnitude), which can also explain the different behavior evidenced above. Nevertheless, the multiple maxima present in the temperature and electronic density profiles reveal a complex behavior of the plasma plume, probably driven by (excitation/ionization/recombination) collisions and electric interactions, leading to the idea of double-layer formation and self-structuring, as evidenced previously in [29–31]. Complementary investigations

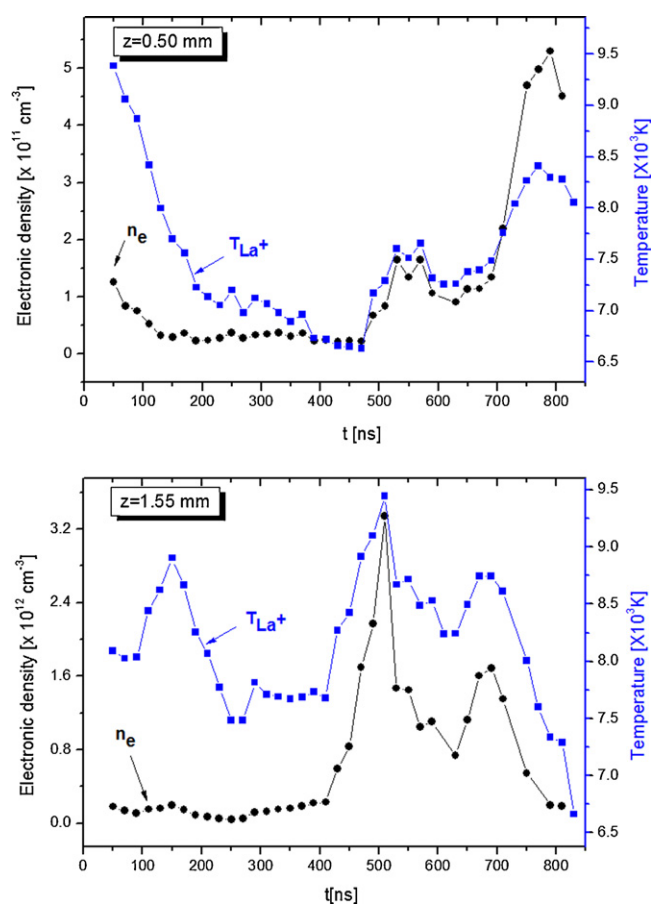


Fig. 7. Excitation temperature and electronic density temporal profiles recorded at $z=0.5$ mm (a) and $z=1.55$ mm (b) from the target surface (laser fluence = 4 J/cm²).

by electrical methods (Langmuir probes and time-of-flight mass spectrometry) are envisaged in order to validate or reject this hypothesis.

4. Conclusions

Dynamics of plasma generated by laser ablation of GLS chalcogenide has been investigated through fast ICCD imaging and time- and space-resolved optical emission spectroscopy. Axial velocities have been derived for several neutral and singly ionized species. Using the relative intensity method, the spatio-temporal evolution of both excitation temperature and electronic density has been investigated. The results evidenced a complex plasma formation with possible self-structuring behavior. These findings may have practical implications for pulsed laser deposition of amorphous chalcogenide thin films. A systematic study (using also electrical characterization methods, e.g. Langmuir probes) on the deposition conditions (including ablation laser pulse duration – ns, ps and fs) is therefore planned.

Acknowledgments

This work was supported by the Conseil Régional Nord Pas de Calais and the Fonds Européen de Développement Economique des Régions in the frame of the CPER CIA project and by a grant of the Romanian National Authority for Scientific Research, CNCS – UEFISCDI, project number PN-II-ID-PCE-2011-3-0650. Financial support from Czech Science Foundation (project No. P106/11/0506) is greatly acknowledged.

References

- [1] V. Nazabal, F. Charpentier, J.-L. Adam, P. Nemeč, H. Lhermite, M.-L. Brandily-Anne, J. Charrier, J.-P. Guin, A. Moréac, *International Journal of Applied Ceramic Technology* 8 (2011) 990.
- [2] M. Frumar, B. Frumarova, T. Wagner, M. Hrdlicka, *Journal of Materials Science: Materials in Electronics* 18 (2007) S169.
- [3] M. Frumar, B. Frumarova, P. Nemeč, T. Wagner, J. Jedelsky, M. Hrdlicka, *Journal of Non-Crystalline Solids* 352 (2006) 544.
- [4] J.S. Sanghera, I.D. Aggarwal, *Journal of Non-Crystalline Solids* 257 (1999) 6.
- [5] S.R. Elliott, *Physics of Amorphous Materials*, 2nd ed., Longman Scientific & Technical, Essex, United Kingdom, 1990.
- [6] M. Guittard, A.M. Loireau-Lozach, F. Berguer, S. Barnier, J. Flahaut, *Journal of Solid State Chemistry* 62 (1986) 191.
- [7] J. Flahaut, M. Guittard, A.M. Loireau-Lozach, *Glass Technology* 24 (1986) 149.
- [8] A. Mairaj, D. Hewak, D.J. Brady, P. Jander, T. Schweizer, Y.W. West, *Electronics Letters* 32 (1996) 384.
- [9] V. Nazabal, M. Cathelinaud, W. Shen, P. Nemeč, F. Charpentier, H. Lhermite, M.-L. Anne, J. Capoulade, F. Grasset, A. Moréac, S. Inoue, M. Frumar, J.L. Adam, M. Lequime, C. Amra, *Applied Optics* 47 (2008) C114.
- [10] A. Zakery, S.R. Elliott, *Optical Nonlinearities in Chalcogenide Glasses and their Applications*, Springer-Verlag, Berlin, Germany, 2007.
- [11] K. Tanaka, K. Shimakawa, *Physica Status Solidi B* 246 (2009) 1744.
- [12] M. Frumar, B. Frumarova, T. Wagner, P. Nemeč, in: A.V. Kolobov (Ed.), *Photo-Induced Metastability in Amorphous Semiconductors*, Wiley-WCH, Weinheim, Germany, 2003, p. 23.
- [13] K.E. Youden, T. Grevatt, R.W. Eason, H.N. Rutt, R.S. Deol, G. Wylangowski, *Applied Physics Letters* 63 (1993) 1601.
- [14] C. Focsa, P. Nemeč, M. Ziskind, C. Ursu, S. Gurlui, V. Nazabal, *Applied Surface Science* 255 (2009) 5307.
- [15] M.S.B. Darby, T.C. May-Smith, R.W. Eason, T. Donnelly, J.G. Lunney, K.D. Rogers, *Applied Surface Science* 254 (2008) 3364.
- [16] S.D. Pangavhane, P. Nemeč, T. Wagner, J. Janča, J. Havel, *Rapid Communications in Mass Spectrometry* 24 (2010) 2000.
- [17] C. Miheșan, S. Gurlui, M. Ziskind, B. Chazallon, G. Martinelli, H. Zeghlache, M. Guignard, V. Nazabal, F. Smektala, C. Focsa, *Applied Surface Science* 248 (2005) 224.
- [18] S. Gurlui, M. Agop, P. Nica, M. Ziskind, C. Focsa, *Physical Review E* 78 (2008) 026405.
- [19] P. Nica, P. Vizureanu, M. Agop, S. Gurlui, C. Focsa, N. Forna, P.D. Ioannou, Z. Borsos, *Japanese Journal of Applied Physics* 48 (2009) 066001.
- [20] C. Ursu, S. Gurlui, C. Focsa, G. Popa, *Nuclear Instruments and Methods in Physics Research Section B* 267 (2009) 446.
- [21] C. Ursu, O.G. Pompilian, S. Gurlui, P. Nica, M. Agop, M. Dudeck, C. Focsa, *Applied Physics A* 101 (2010) 153.
- [22] S. Fähler, K. Sturm, H.-U. Krebs, *Applied Physics Letters* 72 (1998) 1829.
- [23] J. Schou, *Applied Surface Science* 255 (2009) 5191.
- [24] R.L. Kurucz, B. Bell, *Atomic Line Data*, Kurucz CD-ROM No. 23, Smithsonian Astrophysical Observatory, Cambridge, MA, 1995 <http://www.cfa.harvard.edu/amp/ampdata/kurucz23/sekur.html>
- [25] P.W.J.M. Boumans, in: E.L. Grove (Ed.), *Analytical Emission Spectroscopy*, Vol. 1, Part 2, Dekker, New York, 1972.
- [26] H.R. Griem, *Plasma Spectroscopy*, McGraw-Hill, New York, 1964.
- [27] B. Toftmann, J. Schou, T.N. Hansen, J.G. Lunney, *Physical Review Letters* 84 (2000) 3998.
- [28] J.M. Hendron, C.M.O. Mahony, T. Morrow, W.G. Graham, *Journal of Applied Physics* 81 (1997) 2131.
- [29] S. Eliezer, H. Hora, *Physics Reports* 172 (1989) 339.
- [30] S. Gurlui, M. Sanduloviciu, M. Strat, G. Strat, C. Miheșan, M. Ziskind, C. Focsa, *Journal of Optoelectronics and Advanced Materials* 8 (2006) 148.
- [31] P. Nica, M. Agop, S. Gurlui, C. Focsa, *Europhysics Letters* 89 (2010) 65001.



Femtosecond pulsed laser deposition of cobalt ferrite thin films



Georgiana Dascalu^a, Gloria Pompilian^b, Bertrand Chazallon^b, Ovidiu Florin Caltun^{a,*},
Silviu Gurlui^a, Cristian Focsa^b

^a Faculty of Physics, Alexandru Ioan Cuza University, 700506 Iasi, Romania

^b Laboratoire de Physique des Lasers, Atomes et Molécules (UMR CNRS 8523), Université Lille 1 Sciences et Technologies, 59655 Villeneuve d'Ascq cedex, France

ARTICLE INFO

Article history:

Received 15 June 2012

Received in revised form 15 February 2013

Accepted 23 February 2013

Available online 4 March 2013

Keywords:

Femtosecond pulsed laser deposition

Thin films

Ferrite

ABSTRACT

The insertion of different elements in the cobalt ferrite spinel structure can drastically change the electric and magnetic characteristics of CoFe_2O_4 bulks and thin films. Pulsed Laser Deposition (PLD) is a widely used technique that allows the growth of thin films with complex chemical formula. We present the results obtained for stoichiometric and Gadolinium-doped cobalt ferrite thin films deposited by PLD using a femtosecond laser with 1 kHz repetition rate. The structural properties of the as obtained samples were compared with other thin films deposited by ns-PLD. The structural characteristics and chemical composition of the samples were investigated using profilometry, Raman spectroscopy, X-Ray diffraction measurements and ToF-SIMS analysis. Cobalt ferrite thin films with a single spinel structure and a preferential growth direction have been obtained. The structural analysis results indicated the presence of internal stress for all the studied samples. By fs-PLD, uniform thin films were obtained in a short deposition time.

© 2013 Elsevier B.V. All rights reserved.

1. Introduction

Cobalt ferrite is a ferrimagnetic material with an inverse spinel structure which presents the highest magnetocrystalline anisotropy and magnetostriction coefficient among ferrites [1,2]. These properties encourage their use as magnetic material in recording devices, sensors and actuators.

Cobalt ferrite thin films can be obtained by different methods [3–5] but the most promising technique to deposit epitaxial thin films with a preferential crystallographic direction and perpendicular magnetic anisotropy was found to be Pulsed Laser Deposition (PLD) [6,7]. So far, lasers with nanosecond pulse duration (e.g.: excimer and Nd-YAG lasers) have been used for film growth. In this temporal regime the thermal conductivity mechanisms control the ablation threshold fluence and the pulse duration is sufficiently long so that it interacts with the formed plume [8–10]. These ablation processes could explain the presence (in some cases) of large droplets on the surface of thin films obtained by ns-PLD. The presence of these micro-sized particles limits their use in industrial applications or in magnetoelectric multilayer systems where a low roughness is necessary to ensure good mechanical coupling between different phases. A possible solution to this problem can be ensured by ultrafast laser ablation. The femtosecond pulse

duration is smaller than the time needed for the thermalization processes to evolve and the short laser pulse does not interact with the plume. The absence of liquid phase transformation at laser-target interaction can ensure stoichiometric and nano-sized particle ejection. Moreover, it was reported that plasma induced by femtosecond pulsed lasers has a shorter lifetime than the one generated by nanosecond ablation [11]. Another advantage of the ultrafast laser systems is the high repetition rate. Reilly et al. [12] deposited a 140 nm thick film in 20 min using the 74.8 MHz repetition rate of an amplified Ti:sapphire system.

This study was focused on the structural characterization of ferrite thin films obtained by femtosecond PLD with 1 kHz repetition rate. To our knowledge, results on cobalt ferrite thin films deposited by femtosecond PLD were not reported until now. Another aim of this work was to investigate the influence of Gadolinium oxide addition in the target preparation on the structural properties of cobalt ferrite thin films. Due to its large ionic radii, the inclusion of the rare earth element (Gd) into the spinel structure could determine an increase in lattice parameter and an internal stress is induced [13]. Also the high magnetic moment of Gadolinium ions as compared to the iron cations can produce significant changes in magnetic properties.

2. Experimental details

CoFe_2O_4 and $\text{CoFe}_{1.8}\text{Gd}_{0.2}\text{O}_4$ thin films were deposited by fs-PLD using 1.5 cm diameter, 5 mm thick disk targets synthesized by

* Corresponding author. Tel.: +40 232 20 11 74; fax: +40 232 20 11 74.

E-mail addresses: caltun@uaic.ro, ovidiu.caltun@yahoo.com (O.F. Caltun).

solid state chemistry. For the stoichiometric cobalt ferrite target, the powder was obtained by co-precipitation method, pressed and sintered at 1150 °C for 5 h in air atmosphere as described in [14]. For the Gd-doped cobalt ferrite target the powder was obtained by solid state reaction in which the oxides of the constituent elements were mixed in adequate proportions. The resulting powder was calcined at 950 °C for 5 h in air atmosphere and then ball milled. In the sintering stage we used a higher temperature of 1250 °C (5 h, air atmosphere) to facilitate the crystallization process which can be restrained due to the large ionic radius of the rare earth cation.

An experimental set-up originally developed for the study of laser ablation plasma dynamics [8–10,15] has been exploited for fs-PLD of the cobalt ferrite thin films. The targets were placed on a multi-axis manipulator under vacuum (3×10^{-2} Torr) and a 40 fs Ti:Sa laser (Spectra Physics, $\lambda = 800$ nm, repetition rate = 1 kHz, fluence = 0.6 J/cm^2) employed as ablation source was focused at quasi-normal incidence on the target surface. The substrate ((100) monocrystalline silicon) was resistively heated at a temperature of 300 °C and positioned at 16 mm in front of the target. The deposition time was varied between 10 and 20 min. The microstructure characteristics of the thin films synthesized here were compared with the ones observed for other samples previously deposited by nanosecond PLD ($\lambda = 532$ nm, repetition rate = 10 Hz) [13] using the same two targets described above.

The structural characteristics of these thin films were investigated by Raman spectroscopy using an InVia Reflex spectroscope (Renishaw) coupled to an Olympus BXFM free-space microscope. The experiments were carried out at room temperature with an excitation radiation of $\lambda = 514.5$ nm produced by an air-cooled Ar⁺ Laser source (Modu-Laser, Stellar-pro). The Raman analyses were complemented by X-Ray Diffraction (XRD) measurements with a Shimadzu LabX XRD-6000 diffractometer using Cu K α radiation ($\lambda = 1.54059$ Å). In depth profiles of the constituent elements and of their oxides were obtained by Time of Flight–Secondary Ion Mass Spectrometry (ToF-SIMS) using an IonToF V SIMS instrument. A surface of $300 \times 300 \mu\text{m}^2$ was sputtered using a beam of Cs⁺ ions and the secondary ions generated by a beam of 25 keV Bi₃⁺ from a central $100 \times 100 \mu\text{m}^2$ area were analyzed. The thickness of the films was measured using a mechanical contact Veeco Dektak profilometer.

3. Results and discussions

The bulk materials used as targets in the deposition process (undoped and Gd-doped cobalt ferrite) were firstly analyzed by X-ray diffraction. For the undoped cobalt ferrite disk, the XRD pattern indicated the formation of a single spinel structure whereas for the Gd-doped sample, the presence of a second phase of GdFeO₃ was observed in 12% concentration [14]. These results were confirmed by the Raman spectroscopy analysis [13]. Cobalt ferrite has 5 Raman active modes where the peak at 465 cm^{-1} can be assigned to vibrations of the octahedral sublattice and the high-frequency mode at 684 cm^{-1} is determined by the vibrations of the tetrahedral sublattice [16]. For Gd-doped target additional vibrational modes were detected at 139 cm^{-1} , 155 cm^{-1} , 322 cm^{-1} , 477 cm^{-1} and 615 cm^{-1} which can be assigned to the second phase of Gd orthoferrite.

Using these bulk materials thin films of $\text{CoFe}_{2-x}\text{Gd}_x\text{O}_4$ ($x=0, 0.2$) were deposited by PLD in various conditions. Their thicknesses were obtained by contact profilometry measurements, leading to the values listed in Table 1. Mechanical profilometers usually present a detection limit of 10 nm. These results are to be compared with the ones reported in [13] for the thin films deposited by nanosecond PLD. Using a high repetition rate of 1 kHz (and a lower fluence), in 20 min we obtained a thin film with the same thickness as the one deposited in 90 min with a 10 Hz repetition

Table 1
Thin film thickness values obtained by profilometry analysis.

Sample	Repetition rate	Time of deposition (min)	Thickness (nm)
CoFe ₂ O ₄	1 kHz	10	200
CoFe ₂ O ₄		20	320
CoFe _{1.8} Gd _{0.2} O ₄	10 Hz	10	140
CoFe _{1.8} Gd _{0.2} O ₄		20	340
CoFe _{1.8} Gd _{0.2} O ₄		90	350

rate ns Nd-YAG laser. Using the Olympus microscope of the Raman spectroscopy set-up the surface morphology of the thin films was analyzed. The as-obtained images are revealed in Fig. 1, both for fs- and ns-PLD films. For this representation we used the cobalt ferrite films deposited in 10 min and 45 min respectively. As one can easily note, the surface of the ns-PLD film (NF) is affected by the presence of large (micrometer-sized) droplets, while the fs-PLD grown films (FF) present a very smooth surface. This is due to the much lower fluence used in the femtosecond regime (0.6 J/cm^2 , compared to 10 J/cm^2 used in ns-PLD [13]), and also to the intrinsic lower thermal effects induced by the fs-laser ablation, which avoids (or at least greatly reduces) the formation of intermediary liquid-phase droplets during the process. The increased uniformity of the FF sample is confirmed by profilometry measurements. Thickness profiles of the considered thin films are presented in the inset of Fig. 1a and b.

By ToF-SIMS measurements, the distribution of the constituent elements on a $500/500 \mu\text{m}^2$ area was analyzed in positive and

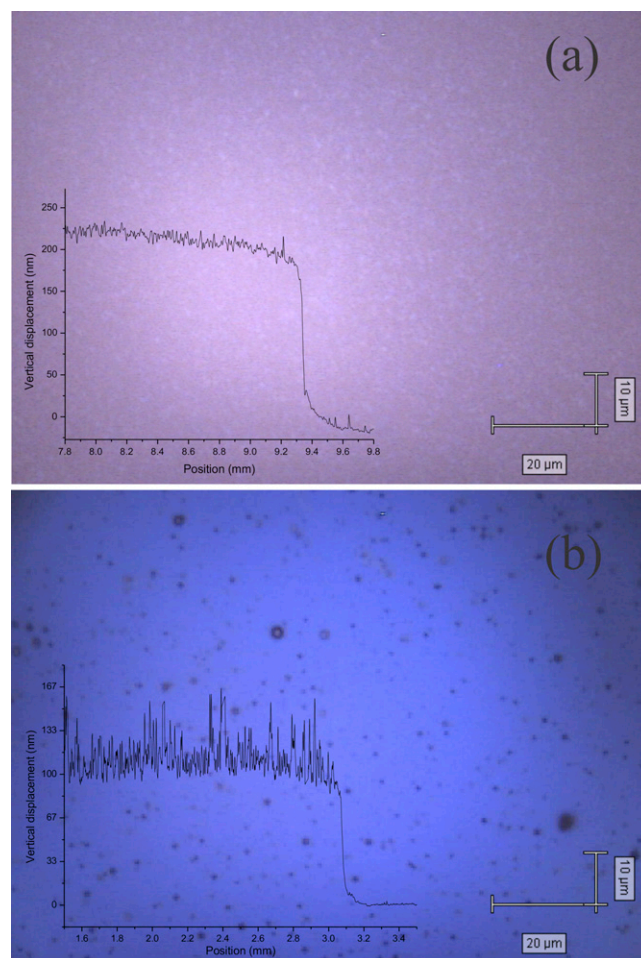


Fig. 1. Microscope images and thickness profiles of: (a) cobalt ferrite FF deposited in 10 min with 0.6 J/cm^2 energy density and (b) cobalt ferrite NF deposited in 45 min with a 10 J/cm^2 fluency.

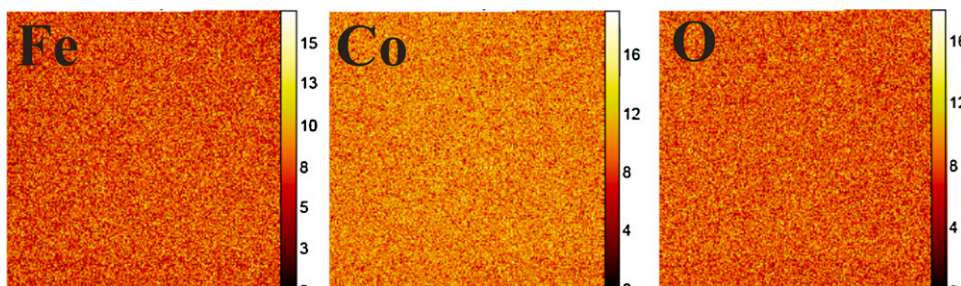


Fig. 2. ToF-SIMS images of the cobalt ferrite FF sample deposited in 20 min. The right colored scale represents mc (maximum counts).

negative polarity. The as-obtained images for the main elements (Fe, Co, O) are presented in Fig. 2. These don't reveal regions with modified chemical properties. By this same method, in depth profiles of the two metals and of their oxides were obtained (Fig. 3). The interdiffusion region between the substrate and the thin film can be explained by the 300 °C temperature used during the deposition process.

The XRD results for the thin films deposited using the fs laser (FF) suggested the formation of a single spinel structure with a preferential crystallographic growth direction. The diffractograms are represented in Fig. 4. The presence of (222) and (400) diffraction lines at slightly decreased 2θ angles indicated an increase in lattice parameter possibly due to structural differences between the substrate and the thin film. When an in situ heating of the substrate is provided, the thermal expansion mismatch can induce internal stress and consequently cell deformation. As the film thickness increases the influence of the substrate properties is reduced and the diffraction lines move closer to the 2θ bulk position. The deposition of highly oriented thin films by femtosecond PLD was reported by other research groups [17]. Chau et al. obtained ZnO thin films with a (002) preferential crystallographic growth direction. Although the presence of Gd cations determined the formation of a second phase of orthoferrite in the target, Raman spectroscopy and XRD analysis performed on the doped thin films indicated the presence of a single cobalt ferrite structure. For each sample, the mean crystallite size was calculated with a Lorentzian profile of the (400) diffraction line using Scherrer formula. We obtained a mean crystallite dimension of 18 nm for the cobalt ferrite thin film deposited in 10 min and a 16 nm one for the sample deposited in 20 min. The error in measuring the crystallite size was below 2 nm.

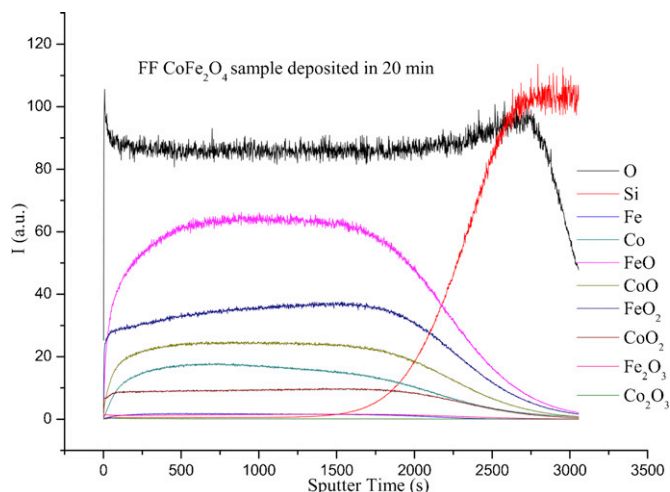


Fig. 3. In depth profiles obtained in negative polarity of the cobalt ferrite FF sample deposited in 20 min.

When Gd cations with large ionic radii are added the crystallinity evolution is restrained. A 14 nm crystallite size was estimated for the $\text{CoFe}_{1.8}\text{Gd}_{0.2}\text{O}_4$ thin film deposited in 20 min. Similarly, the XRD pattern of NF Gd-doped cobalt ferrite sample revealed the formation of a single spinel structure, but the presence of a more intense (311) diffraction line in the diffractogram suggested a polycrystalline film growth. The crystallite size estimated from the Lorentzian profile of the (311) peak was below 10 nm [13]. Due to the high $10\text{J}/\text{cm}^2$ laser fluence used for these thin films, large particles were ejected from the target. When deposited on the substrate, their dimensions and polycrystalline nature influenced the growth mechanisms and determined the formation of a thin sample with no preferential crystallographic structure. Unlike the structural results obtained for the FF samples, for the ferrite thin films deposited using a nanosecond Nd-YAG laser a constrained

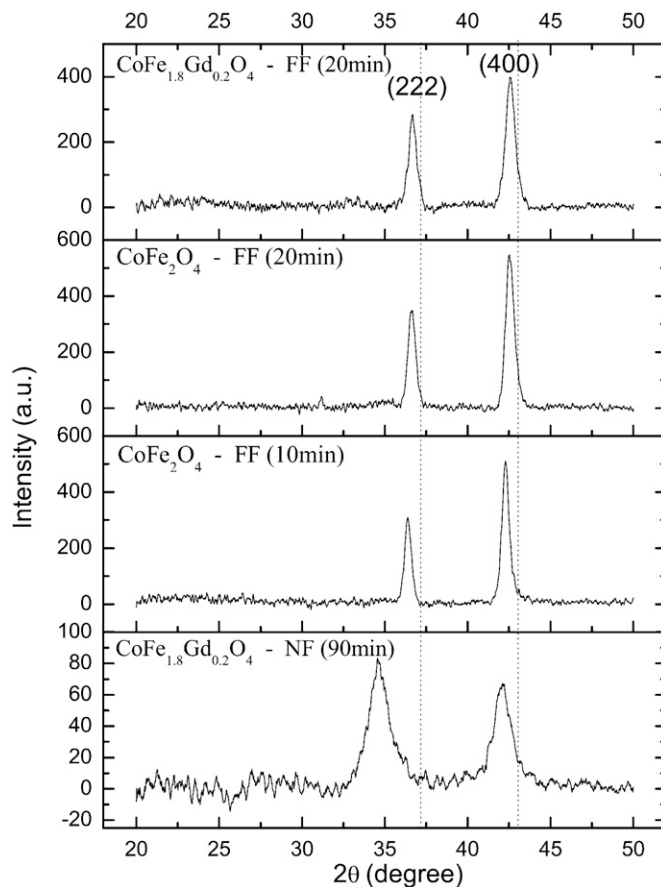


Fig. 4. XRD patterns of the thin films deposited using the fs laser and of Gd doped NF deposited in 90 min. the dotted lines represent the 2θ position of the (222) and (400) diffraction peaks corresponding to the target.

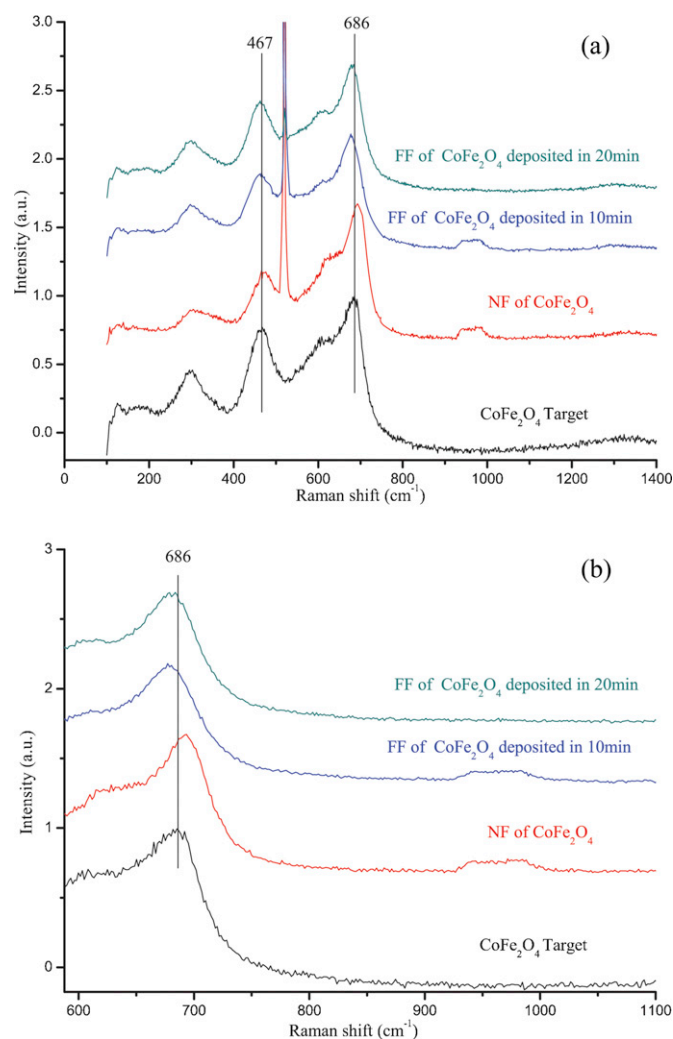


Fig. 5. Raman spectra of the cobalt ferrite target and thin films obtained in different conditions (a) and an enhanced image of the 600–1100 cm^{-1} region of the spectra (b).

spinel structure was observed [13]. The structural properties of the thin films were influenced by the laser characteristics. The induced mechanical tensions depend on the fluence used for ablation. For the FF samples, the small particles that arrive at the substrate surface have the tendency to relax while for the NF sample a contraction of the micro-sized droplets is implied. Using a low fluence a fine particle ejection can be achieved.

A distortion of the spinel phase was also indicated by Raman spectroscopy analysis where the peak corresponding to the vibrations of the tetrahedral sublattice presented a shift to lower frequencies. As the length of the chemical bond between two elements gets larger, the frequency and thus the wavenumber decrease. In contrast with these results, for the stoichiometric cobalt ferrite NF samples we observed a shift of the same 684 cm^{-1} peak towards higher frequencies which indicated a contraction of the unit cell (Fig. 5). The distinct structural characteristics of the NF and FF samples can be explained by the different ablation processes that take place in the two temporal regimes. The low energy of the femtosecond pulse can ensure the ejection of particles with small dimensions and thus a more uniform thin film can be deposited. Combined with the in situ heating of the substrate, the temperature and dimension of the ejected particles that are deposited can induce different mechanical tensions. The structural analysis of the FF $\text{CoFe}_{1.8}\text{Gd}_{0.2}\text{O}_4$ sample revealed an increased cell edge of the

spinel lattice which can be explained by the insertion of the rare earth element with large ionic radius into the cubic closed packed structure.

Although the structural characterization results indicated a preferential growth direction for the FF samples, preliminary magnetic measurements did not reveal the presence of a magnetic anisotropy. Using a Vibrating Sample Magnetometer, hysteresis curves for both in plane and out of plane configurations were obtained. We plan to perform a detailed magnetic analysis with a torsion magnetometer which can offer more information on magnetic moment orientation.

4. Conclusions

Undoped and Gd-doped cobalt ferrite thin films were deposited by PLD using a femtosecond laser source with low fluence and 1 kHz repetition rate for target ablation. The structural characterization techniques used for this study revealed that for the bulk material, Gd cation addition determined the formation of a second phase with a perovskite type structure. The XRD and Raman spectroscopy measurements conducted at room temperature on the thin films gave evidence of a distorted spinel phase. No residual phases were detected. The enlarged lattice parameter observed for all FF samples was correlated to the shift of the 684 cm^{-1} Raman peak to lower frequencies. By femtosecond laser ablation, in 10 min we obtained cobalt ferrite thin films with improved uniformity and 200 nm thickness. Due to the low fluence used for ejection, the deposition of micro-sized particles was avoided and the formation of a crystalline thin film with a preferential growth direction was achieved. ToF-SIMS analysis revealed a uniform distribution of the constituent elements and of their oxides on the surface and in the volume. These results encourage the use of fs-PLD for thin film deposition. Due to the short laser pulse, the material melting stage observed at the interaction between the nanosecond pulsed laser with the target is avoided and an instant vaporization of the material occurs. The ablation mechanisms from this temporal regime allow the formation of uniform thin films with preferential crystallographic growth directions. The high repetition rate ensures short deposition times and represents an advantage of technological interest.

Acknowledgements

This work was supported by the Romanian National Authority for Scientific Research, CNCS-UEFISCDI, project number PN-II-ID-PCE-2011-3-0650. The authors would like to thank Nicolas Nuns for ToF-SIMS measurements.

References

- [1] T. Dhakal, D. Mukherjee, R. Hyde, P. Mukherjee, M.H. Phan, H. Srikanth, S. Witanachchi, Magnetic anisotropy and field switching in cobalt ferrite thin films deposited by pulsed laser ablation, *Journal of Applied Physics* 107 (2010) 053914.
- [2] S.D. Bhame, P.A. Joy, Magnetic and magnetostrictive properties of manganese substituted cobalt ferrite, *Journal of Physics D: Applied Physics* 40 (2007) 3263–3267.
- [3] F. Oudrhiri-Hassani, L. Presmanes, A. Barnabé, P. Tailhades, Microstructure, porosity and roughness of RF sputtered oxide thin films: Characterization and modeling, *Applied Surface Science* 254 (2008) 5796–5802.
- [4] J.H. Yin, B.H. Liu, J. Ding, Y.C. Wang, High coercivity in nanostructured Co-ferrite thin films, *Bulletin of Materials Science* 29 (2006) 573–580.
- [5] F. Zhang, S. Kantake, Y. Kitamoto, M. Abe, Spin-spray ferrite-plated Co ferrite films with high coercivity for perpendicular magnetic recording media, *IEEE Transactions on Magnetics* 35 (1999) 2751–2753.
- [6] P.C. Dorsey, P. Lubitz, D.B. Chrisey, J.S. Horwitz, CoFe_2O_4 thin films grown on (100) MgO substrates using pulsed laser deposition, *Journal of Applied Physics* 79 (1996) 6338–6340.
- [7] M. Ning, J. Li, C.K. Ong, S.J. Wang, High perpendicular coercive field of (100)-oriented CoFe_2O_4 thin films on Si(100) with MgO buffer layer, *Journal of Applied Physics* 103 (2008) 013911.

- [8] S. Gurlui, M. Sanduloviciu, M. Strat, G. Strat, C. Mihasan, M. Ziskind, C. Focsa, Dynamic space charge structures in high fluence laser ablation plumes, *Journal of Optoelectronics Advance Materials* 8 (2006) 148–151.
- [9] P. Nica, P. Vizureanu, M. Agop, S. Gurlui, C. Focsa, N. Forna, P.D. Ioannou, Z. Boros, Experimental and theoretical aspects of aluminum expanding laser plasma, *Japanese Journal of Applied Physics* 48 (2009) 066001.
- [10] C. Ursu, S. Gurlui, C. Focsa, G. Popa, Space- and time-resolved optical diagnosis for the study of laser ablation plasma dynamics, *Nuclear Instruments Methods B* 267 (2009) 446–450.
- [11] X. Zenga, X. Mao, R. Greif, R.E. Russo, Experimental investigation of ablation efficiency and plasma expansion during femtosecond and nanosecond laser ablation of silicon, *Applied Physics A* 80 (2005) 237–241.
- [12] A. Reilly, C. Allmond, S. Watson, J. Gammon, J. Gi Kim, Pulsed laser deposition with a high average power free electron laser: Benefits of subpicosecond pulses with high repetition rate, *Journal of Applied Physics* 93 (2003) 3098.
- [13] G. Dascalu, G. Pompilian, B. Chazallon, V. Nica, O.F. Caltun, S. Gurlui, C. Focsa, Rare earth doped cobalt ferrite thin films deposited by PLD, *Applied Physics A* 110 (2013) 915–922.
- [14] G. Dascalu, T. Popescu, M. Feder, O.F. Caltun, Structural, electric and magnetic properties of $\text{CoFe}_{1.8}\text{RE}_{0.2}\text{O}_4$ (RE = Dy, Gd, La) bulk materials, *Journal of Magnetism and Magnetic Materials* 333 (2013) 69–74.
- [15] S. Gurlui, M. Agop, P. Nica, M. Ziskind, C. Focsa, Experimental and theoretical investigations of a laser-produced aluminum plasma, *Physical Reviews E* 78 (2008) 026405.
- [16] J. Barbosa, B.G. Almeida, J.A. Mendes, A.G. Rolo, J.P. Araújo, J.B. Sousa, Nanogranular BaTiO_3 - CoFe_2O_4 thin films deposited by pulsed laser ablation, *Journal of Applied Physics* 101 (2007) 09M101.
- [17] J.L.H. Chau, M.C. Yang, T. Nakamura, S. Sato, C.C. Yang, C.W. Cheng, Fabrication of ZnO thin films by femtosecond pulsed laser deposition, *Optics & Laser Technology* 42 (2010) 1337–1339.

Experimental and theoretical investigations of plasma multiple double layers and their evolution to chaos

This content has been downloaded from IOPscience. Please scroll down to see the full text.

2013 Plasma Sources Sci. Technol. 22 035007

(<http://iopscience.iop.org/0963-0252/22/3/035007>)

View [the table of contents for this issue](#), or go to the [journal homepage](#) for more

Download details:

IP Address: 85.122.26.121

This content was downloaded on 12/10/2013 at 09:19

Please note that [terms and conditions apply](#).

Experimental and theoretical investigations of plasma multiple double layers and their evolution to chaos

D G Dimitriu¹, M Aflori², L M Ivan¹, V Radu¹, E Poll¹ and M Agop^{3,4}

¹ Faculty of Physics, 'Alexandru Ioan Cuza' University, 11 Carol I Blvd., 700506 Iasi, Romania

² Romanian Academy, Petru Poni Institute of Macromolecular Chemistry, 41A Grigore Ghica Voda Alley, 700487 Iasi, Romania

³ Department of Physics, 'Gh. Asachi' Technical University, 59A Mangeron Blvd., 700050 Iasi, Romania

⁴ Laboratoire de Physique des Lasers, Atomes et Molécules (UMR 8523), Université des Sciences et Technologies de Lille, Villeneuve d'Ascq cedex 59655, France

E-mail: dimitriu@uaic.ro

Received 3 February 2013, in final form 4 February 2013

Published 7 May 2013

Online at stacks.iop.org/PSST/22/035007

Abstract

We report experimental results showing that a discharge plasma, which self-structures as concentric multiple double layers, is capable of evolving towards chaos through a cascade of spatio-temporal sub-harmonic bifurcations when the applied constraint (in the form of voltage applied on a supplementary electrode immersed in the plasma) is gradually increased. By considering that the plasma particles (electrons, ions and neutrals) move on fractal curves, a theoretical model able to explain both the plasma self-structuring and the scenario of evolution to chaos is constructed. The experimental results were found to be in good agreement with those obtained from the theoretical model.

(Some figures may appear in colour only in the online journal)

1. Introduction

Concentric multiple double layers are complex non-linear potential structures in plasmas, consisting of two or more double-layer shells attached to the anode of a dc glow discharge [1–6] or to a positively biased electrode immersed in a plasma [7–10]. They appear as several bright and concentric shells attached to the electrode (as shown in figure 1(a)). The successive double layers are located precisely at the abrupt changes in luminosity between two adjacent plasma shells. The number of layers depends on the background gas, on its pressure, on the electrode voltage and on the discharge current [6, 8]. The axial profile of the plasma potential has a stair step shape, with potential jumps close to the ionization potential of the working gas [3, 7, 10]. Simultaneously with each new double-layer appearance, a current jump is recorded in the current–voltage characteristic of the exciting electrode [7]. See, for example, the current–voltage characteristic of the exciting electrode in figure 2, recorded under the experimental conditions in which a multiple double-layer structure consisting of two double layers was obtained. Thus,

the current collected by the electrode increases with the number of double layers existing in the multiple double-layer structure. At high values of the voltage applied to the electrode, the multiple double-layer structure passes into a dynamic state, which consists of periodic disruptions and re-aggregations of the constituent double layers [10, 11]. In this case, the luminous shells become broader and diffuse (see the photo in figure 1(b)), because of the space–time behavior of the constituent double layers. Thus, according to [12], in the dynamic state the double layer moves away from the electrode for a short distance and after this it disrupts and re-aggregates in the initial position (it appears as a periodic shelling).

Experimental investigations have proven the important role of elementary processes such as electron–neutral impact excitations and ionizations in the formation and dynamics of the multiple double layer [7, 11].

Different models were proposed for such structures, in which the appearance of the double layers was explained through a bifurcation [13], or the double layers were assimilated with Turing-type structures [14].

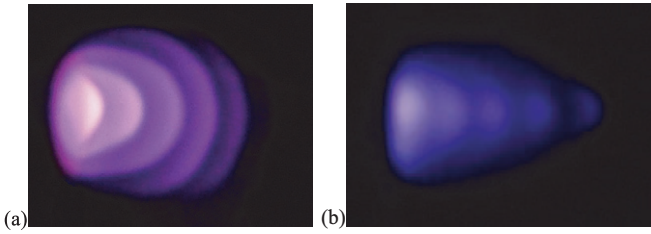


Figure 1. Multiple double layers in a plasma in (a) static and (b) dynamic states.

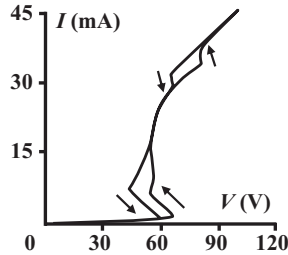


Figure 2. Current–voltage characteristic of the exciting electrode, recorded under the conditions in which a multiple double-layer structure consisting of two double layers develops.

In many systems where deterministic chaos arises, spatial and temporal structures were also experimentally observed. For time scales large with respect to the inverse of the maximum Lyapunov exponent, deterministic trajectories can be replaced by families of potential trajectories and the concept of definite positions by that of probability density. This allows the description of chaos in a stochastic way by a diffusion process as described in [15]. By considering that the particle movement takes place on continuous but non-differentiable curves (fractal curves), the scale relativity theory (SRT) approaches the chaotic effects in the same way as in [16], except for diffusion, which becomes a spatio-temporal scale-dependent process (see [17, 18] for details).

Here we report experimental results revealing how the electrically conductive plasma can self-structure in the form of concentric multiple double layers. We show that these new structures evolve toward chaos through a cascade of spatio-temporal sub-harmonic bifurcations when the applied constraint in the form of voltage applied on a supplementary electrode immersed into the plasma increases. The fast Fourier transforms (FFTs) of the current oscillations collected by the electrode illustrate the appearance of new sub-harmonics of the fundamental frequency simultaneously with every appearance of a new double-layer structure (as part of the multiple double-layer structure) in the dynamic state. A theoretical model based on SRT is developed, and its results are found to be in good agreement with the experimental data. Thus, the model describes both the self-structuring of a constrained (in the form of potential applied on the electrode) plasma as multiple double-layer structures and its evolution to chaos through a cascade of spatio-temporal bifurcations.

2. Experimental results

The experiments were performed in a plasma diode, schematically presented in figure 3. The plasma is created

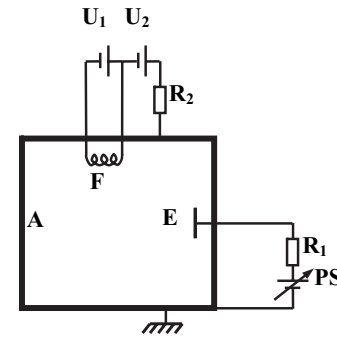


Figure 3. Schematic of the experimental setup (F—filament, A—anode, E—supplementary electrode, P—cylindrical probe, U_1 —power supply for heating the filament, U_2 —power supply for the discharge, PS—power supply for supplementary electrode bias, R_1 , R_2 —load resistors).

by an electrical discharge between the hot filament (marked by F in figure 3) as a cathode and the grounded tube (made of non-magnetic stainless steel) as an anode. The plasma was pulled away from equilibrium by gradually increasing the voltage applied to a tantalum disk electrode (marked by E in figure 3) of diameter 1 cm, under the following experimental conditions: argon pressure $p = 10^{-2}$ mbar, plasma density $n_{pl} \approx 10^9$ cm $^{-3}$ and electron temperature $kT_e \approx 2$ eV.

When the voltage on the electrode reaches $V_E \approx 55$ V, a double-layer structure appears in front of the electrode (see the photo in figure 4(a)). Due to the experimental conditions, this structure appears directly in a dynamic state, as explained in [19]. Such a dynamic state of a double layer was extensively described in [20–23]. The oscillations of the current collected by the electrode, their FFT and the reconstructed attractor of the system dynamics in the state space (by the time delay method, extensively described in [24]) are shown in figures 5(a), (b) and (c), respectively. By a further increase in the voltage on the electrode, new double layers develop in front of the electrode, giving rise to a dynamic multiple double-layer structure (see photos in figures 4(b)–(e)). Simultaneously with every new double-layer formation, a new sub-harmonic appears in the FFT spectrum of the current oscillations collected by the electrode, the corresponding attractor becoming more and more complex (see figure 5, second and third columns). Thus we recorded, in fact, spatio-temporal bifurcations in the plasma system (sudden changes in the spatial symmetry and in the temporal dynamics of the plasma system). At high values of the applied potential, the plasma system passes into a chaotic state, characterized by uncorrelated and intermittent oscillations (see figures 5(s)–(u), respectively).

Figures 6(a) and (b) show the axial profiles of the electric field and electric charge density in front of the electrode (the electrode is placed at the position $x = 0$ on the graphs), respectively, obtained as the first and second derivatives of the axial profile of the plasma potential, which was experimentally recorded with the help of an axially movable emissive probe. The two graphs correspond to the situation in which a multiple double-layer structure consisting of two double layers exists in front of the electrode in a static state (no oscillations of the current collected by the electrode being recorded). The double

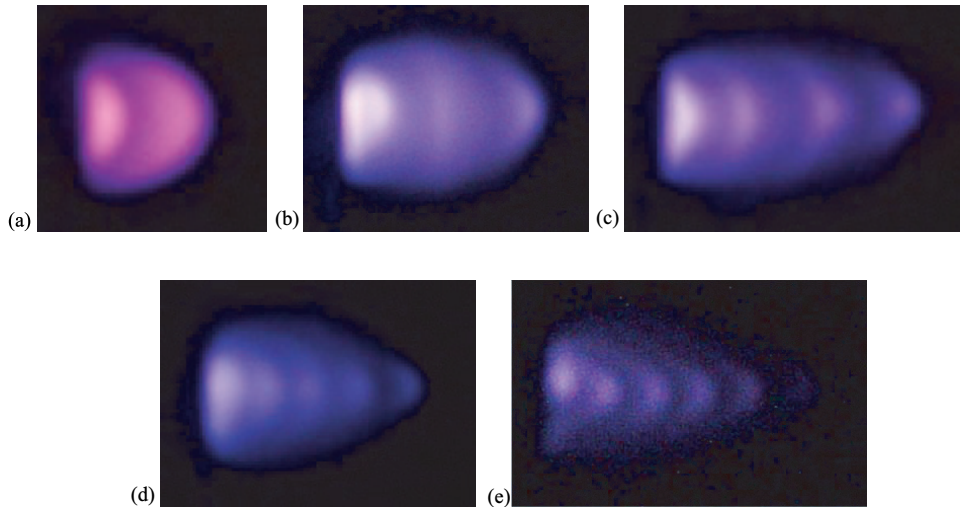


Figure 4. Photos of the multiple double-layer structure at different stages (at different potentials applied on the electrode) of its formation.

layers are placed in the positions where the electric field has the maximum values, marked by arrows in figure 6(a). From figure 6(b) we observe that the space charge density decreases as the distance to the electrode increases.

The stability of a double layer is ensured by the balance between the production of electrons and positive ions through electron–neutral impact ionizations and excitations and the particle losses by recombination and diffusion (see [7, 10, 25] for details). At high values of the current flowing through the structure, this equilibrium is lost and the double layer passes into a dynamic state. When the double layer disrupts, the initially trapped particles (electrons and positive ions) are released and move toward the electrodes as bunches. In the case of multiple double layers, the free particles have to pass through the other double layers and can affect their dynamics. Then, the dynamics of the multiple double-layer structure becomes more complex and spatio-temporal bifurcation appears (sub-harmonics in the current oscillation spectrum and a spatial bifurcation of the plasma in front of the electrode are observed). This resembles the well-known Feigenbaum scenario of transition to chaos by cascades of period-doubling bifurcations [26], but is not the case because in our experiment we did not record period-doubling bifurcations, except for the first one, but sub-harmonic bifurcations. The final plasma system state is a chaotic one, consisting of uncorrelated and intermittent oscillations with a broad spectrum and many peaks being present, which corresponds to the unstable periodic dynamics of the multiple double-layer structure.

3. Theoretical results

The analysis of the complex dynamics of a discharge plasma can be simplified by supposing that it displays chaotic behavior, self-similarity and strong fluctuations on all possible scales [16–18, 27–29]. This means that the plasma particles (electrons, ions and neutrals) move on continuous but non-differentiable curves, i.e. fractal curves (for example the Koch curve, Peano curve or Weierstrass curve [27–29]). Let us

explain this assertion. Between two successive collisions the trajectory of any particle is a straight line, while it becomes non-differentiable at the impact points (there are left and right derivatives at these points [16, 17, 27]). Considering that all the collision points constitute an innumerable set of points, it results in the trajectories becoming continuous and non-differentiable curves (fractal curves). Once such a hypothesis is accepted, some specific consequences through SRT are stated (we will adapt these to the dynamics of a discharge plasma) [16–18, 27]:

- (i) A continuous and non-differentiable curve is explicitly scale-dependent. Its length tends to infinity when the scale interval tends to zero. Since the generalization of this theorem to three dimensions is straightforward, it follows that a continuous and non-differentiable space is fractal, under the general meaning of scale divergence [28].
- (ii) Non-differentiability (through fractality) involves the use of fractal functions to describe the dynamics of a discharge plasma. This means that the quantities describing the dynamics depend on both coordinate (x), time (t) and the scale resolution (dt), in the general form [17, 27]

$$F(x, t, dt) = P(x, t) + Q(x, t, dt) \quad (1)$$

where $P(x, t)$ is a differentiable function, while

$$Q(x, t, dt) = \bar{Q}(x, t)(dt)^\tau \quad (2)$$

is a non-differentiable function and τ a parameter depending on the fractal dimension D_F of the movement curve. We can distinguish the following limit dynamic regime:

- asymptotic regime for small-scale resolutions $dt \ll 1$ and constant τ , a case in which relation (1) reduces to the power-type law

$$F(x, t, dt) \rightarrow \bar{Q}(x, t)(dt)^\tau; \quad (3)$$

in particular, the Child–Langmuir conduction, $j \sim V^{3/2}$, is a power-type law;

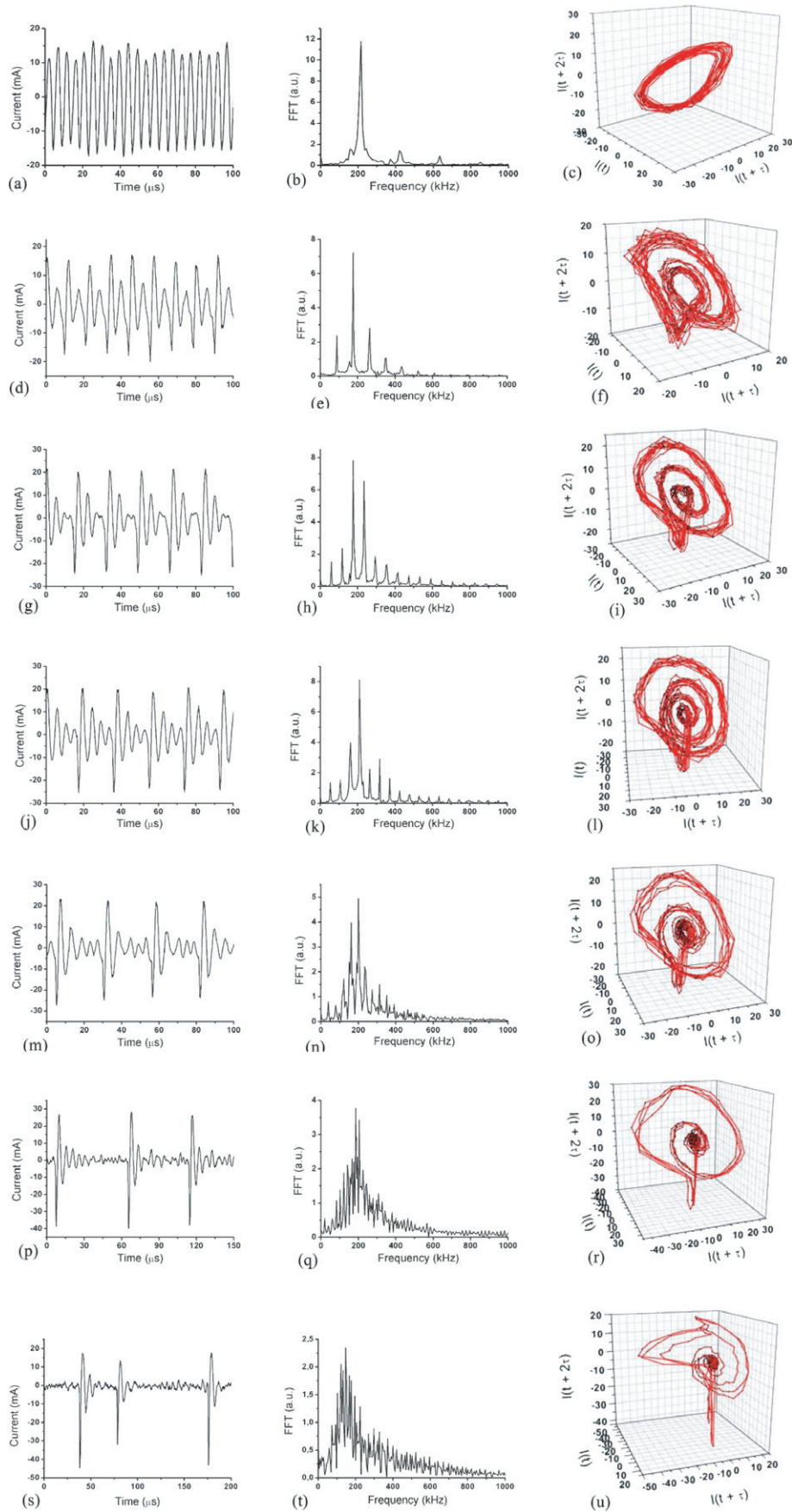


Figure 5. Oscillations of current (first column), their FFTs (second column) and the attractor of the plasma system dynamics in the reconstructed state space (third column), at different increasing values of the voltage applied to the electrode.

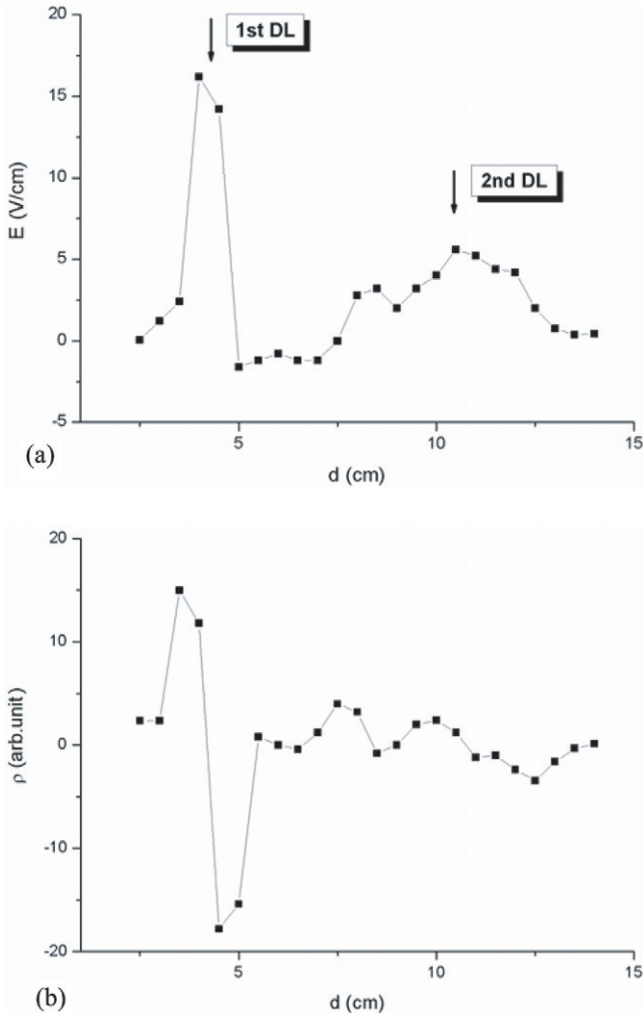


Figure 6. Axial profiles of (a) the electric field (the positions of the individual double layers are marked by arrows) and (b) charge density, respectively, in front of the electrode.

- asymptotic regime for large-scale resolutions $dt \gg 1$ and constant τ , a case in which relation (1) involves

$$F(x, t, dt) \rightarrow P(x, t); \quad (4)$$

for example, Ohmic conduction is such a regime. According to [30] and through relations (1) and (2), we can choose the fractal normalized current–voltage characteristic in the form

$$\bar{\phi} = \bar{I} \left(1 + \frac{\bar{a}}{1 + \bar{I}^2} \right), \quad (5)$$

where $\bar{\phi}$ is the fractal normalized voltage, \bar{I} is the fractal normalized current and \bar{a} is a parameter depending on the scale resolution. This relation induces a conduction bistability (see figure 7) as follows:

- according to [30], the restriction $\bar{a} \geq 8$ implies the bistability;
- the value of \bar{a} sets the scale resolution through the ionization and recombination rates;

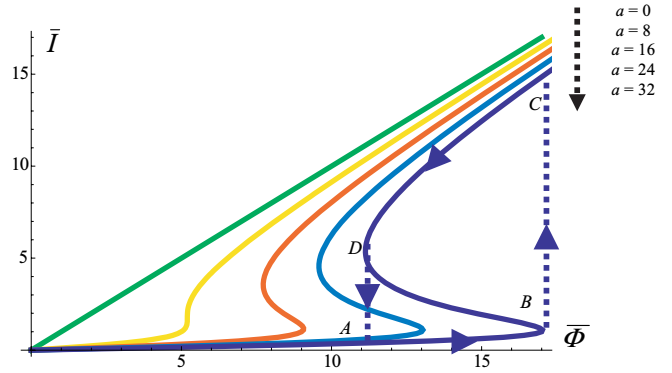


Figure 7. Theoretical dependence of the fractal normalized current on the fractal normalized potential.

- once \bar{a} is fixed (with $\bar{a} \geq 8$), for values of the fractal normalized current in the interval AB on the characteristic (see figure 7), the fractal normalized voltage can have two distinct stable values;
- the conduction bistability is associated with the negative differential resistance (or hysteresis);
- since in relation (5) $\bar{\phi}$ and \bar{I} are fractal functions, they show the property of self-similarity. Consequently, the conduction bistability from figure 7 can be found at any scale resolution (i.e. for different ionization and recombination rates). Thus, we state the possible correspondence between the multiplicity order of the double layer and that of the conduction bistability (see the experimental hysteresis cycles from figure 2 for double layers of multiplicity two).

- (iii) There is an infinity of fractal trajectories (geodesics) relating any couple of points on all scales. In order to account for the infinity of geodesics, for their fractality and for two-valuedness of the derivative, which all come from the non-differentiable geometry of the space (for details see [17, 27]), one therefore adopts a generalized statistical fluid-like description (fractal fluid).

In fact, according to SRT, the dynamics of the plasma discharge are described by the complex operator [31–34]

$$\frac{\hat{d}}{dt} = \frac{\partial}{\partial t} + \hat{V} \cdot \nabla - iD(dt)^{(2/D_F)-1} \Delta, \quad (6)$$

where \hat{V} is the complex speed field

$$\hat{V} = V_D - iV_F, \quad (7)$$

V_D is the standard classical speed (differentiable speed), which is independent of scale resolution, while the imaginary part, V_F , is a new quantity arising from non-differentiability (the fractal speed), which is resolution-dependent, D is a structure coefficient, characteristic of the fractal–non-fractal transition [17, 27]. In the standard models [35, 36], the movements of the plasma particles take place on continuous and differentiable curves, so that its dynamics are described by the classic operator d/dt .

Applying the operator (6) to the complex speed field (7) and accepting a generalized inertial principle, we obtain a

Navier–Stokes-type equation:

$$\frac{\hat{d}\hat{V}}{dt} = \frac{\partial\hat{V}}{\partial t} + (\hat{V} \cdot \nabla)\hat{V} - iD(dt)^{(2/D_F)-1} \Delta\hat{V} = 0. \quad (8)$$

Equation (8) means that at any point of a fractal path, the local acceleration term, $\partial_t \hat{V}$, the non-linear (convective) term, $(\hat{V} \cdot \nabla)\hat{V}$, and the dissipative one, $\Delta\hat{V}$, balance. Moreover, the behaviors of the plasma are of viscoelastic or of hysteretic type, i.e. it has memory (see also the consequence (ii) above). Such a result is in agreement with the opinion given in [31–34]: a plasma can be described by the Kelvin–Voight or Maxwell rheological model with the aid of complex quantities, e.g. the complex speed field, \hat{V} , the imaginary viscosity coefficient, $iD(dt)^{(2/D_F)-1}$, etc.

If the motions of the discharge plasma are irrotational,

$$\nabla \times \hat{V} = 0, \quad \nabla \times \mathbf{V}_D = 0, \quad \nabla \times \mathbf{V}_F = 0, \quad (9a-c)$$

we can choose \hat{V} of the form

$$\hat{V} = -2iD(dt)^{(2/D_F)-1} \nabla \ln \psi. \quad (10)$$

For $\psi = \sqrt{\rho}e^{iS}$, with $\sqrt{\rho}$ the amplitude and S the phase of ψ , the complex speed field (7) takes the explicit form

$$\hat{V} = 2D(dt)^{(2/D_F)-1} \nabla S - iD(dt)^{(2/D_F)-1} \nabla \ln \rho, \quad (11)$$

$$\mathbf{V}_D = 2D(dt)^{(2/D_F)-1} \nabla S, \quad (12)$$

$$\mathbf{V}_F = D(dt)^{(2/D_F)-1} \nabla \ln \rho. \quad (13)$$

By substituting (11)–(13) into (8) and separating the real and imaginary parts, up to an arbitrary phase factor which may be set at zero by a suitable choice of the phase of ψ , we obtain

$$\frac{\partial \mathbf{V}}{\partial t} + (\mathbf{V}_D \cdot \nabla)\mathbf{V}_D = -\nabla Q, \quad (14)$$

$$\frac{\partial \rho}{\partial t} + \nabla \cdot (\rho \mathbf{V}_D) = 0, \quad (15)$$

with Q the specific fractal potential

$$\begin{aligned} Q &= -2D^2(dt)^{(4/D_F)-2} \frac{\Delta\sqrt{\rho}}{\sqrt{\rho}} \\ &= -\frac{\mathbf{V}_F^2}{2} - D(dt)^{(2/D_F)-1} \nabla \cdot \mathbf{V}_F. \end{aligned} \quad (16)$$

Equation (14) represents the law of momentum conservation, while equation (15) represents the law of density conservation. Through the fractal speeds field, \mathbf{V}_F , the specific fractal potential, Q , is a measure of non-differentiability of the plasma particle trajectories, i.e. of their chaoticity. The presence of an external field with a specific scalar potential U modifies the law of momentum conservation in the form

$$\frac{\partial \mathbf{V}_D}{\partial t} + (\mathbf{V}_D \cdot \nabla)\mathbf{V}_D = -\nabla(Q + U). \quad (17)$$

Equations (14)–(16) define the fractal hydrodynamics. A correspondence with the classical hydrodynamics is established in the appendix.

Further, using equations (14) and (15) for an axial symmetry, we will analyze the dynamics of a discharge plasma by choosing expression (A.10) from the appendix for the fractal potential and considering that the movements of the plasma particles take place on fractal curves with $D_F = 2$ (for details see [17, 27–30]). The external constraint on the discharge plasma, in the form of potential applied on the electrode, is specified by adequate initial and boundary conditions. Let us introduce the normalized quantities:

$$\begin{aligned} \omega t = \tau, \quad kr = \xi, \quad kz = \eta, \quad \frac{V_{Dr}}{c} = V_\xi, \quad \frac{V_{Dz}}{c} = V_\eta, \\ \rho/\rho_0 = N, \quad \frac{kc}{\omega} = 1, \end{aligned} \quad (18a-g)$$

where ω is the plasma pulsation, k is the inverse of the Debye length, c is the ion-acoustic speed and ρ_0 is the equilibrium plasma density. Then, equations (14) and (15) become

$$\frac{\partial}{\partial \tau}(NV_\xi) + \frac{1}{\xi} \frac{\partial}{\partial \xi}(\xi NV_\xi^2) + \frac{\partial}{\partial \eta}(NV_\xi V_\eta) = -\frac{\partial N}{\partial \xi}, \quad (19)$$

$$\frac{\partial}{\partial \tau}(NV_\eta) + \frac{1}{\xi} \frac{\partial}{\partial \xi}(\xi NV_\xi V_\eta) + \frac{\partial}{\partial \eta}(NV_\eta^2) = -\frac{\partial N}{\partial \eta}, \quad (20)$$

$$\frac{\partial N}{\partial \tau} + \frac{1}{\xi} \frac{\partial}{\partial \xi}(\xi NV_\xi) + \frac{\partial}{\partial \eta}(NV_\eta) = 0. \quad (21)$$

For the numerical integration we shall impose the initial conditions

$$\begin{aligned} V_\xi(0, \xi, \eta) = 0, \quad V_\eta(0, \xi, \eta) = 0, \quad N(0, \xi, \eta) = 1/5, \\ 1 \leq \xi \leq 2, \quad 0 \leq \eta \leq 1, \end{aligned} \quad (22a-e)$$

as well as the boundary conditions

$$\begin{aligned} V_\xi(\tau, 1, \eta) = V_\xi(\tau, 2, \eta) = 0, \\ V_\eta(\tau, 1, \eta) = V_\eta(\tau, 2, \eta) = 0, \\ V_\xi(\tau, \xi, 0) = V_\xi(\tau, \xi, 1) = 0, \\ V_\eta(\tau, \xi, 0) = V_\eta(\tau, \xi, 1) = 0, \\ N(\tau, 1, \eta) = N(\tau, 2, \eta) = 1/5, \\ N(\tau, \xi, 0) = \frac{1}{10} \exp \left[-\left(\frac{\tau - 1/5}{1/5} \right)^2 \right] \\ \times \exp \left[-\left(\frac{\xi - 3/2}{1/5} \right)^2 \right], \\ N(\tau, \xi, 1) = 1/5. \end{aligned} \quad (23a-g)$$

The equation system (19)–(21) with the initial conditions (22a–e) and the boundary conditions (23a–g) was numerically solved using the finite differences [37]. Figures 8–10 show the three-dimensional (3D) dependences (figures 8(a)–10(a)) and two-dimensional (2D) contours (figures 8(b)–10(b)) of the normalized density N and the normalized speeds V_ξ and V_η , respectively, on the normalized coordinates ξ and η at the normalized time value $\tau = 0.74$. Using these numerical solutions, the theoretical profiles of the electrical field and density, respectively, are given in figures 11(a) and (b).

This results in the following:

- generation of multiple structures in the plasma (figures 8(a) and (b)), corresponding to the multiple double layers, such as those shown in figure 4;

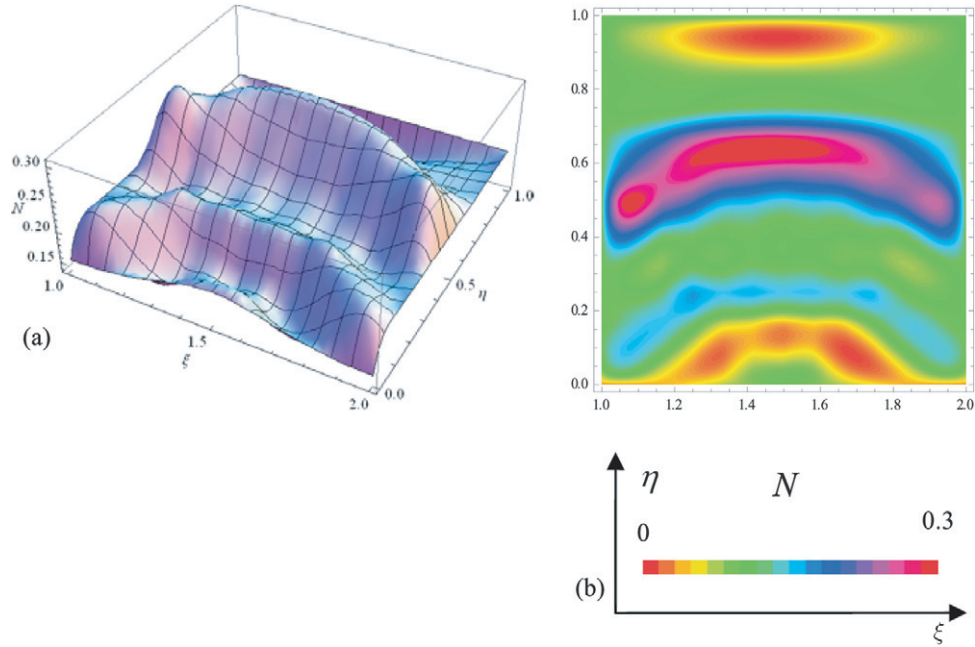


Figure 8. (a) 3D dependence of the normalized density field N on the normalized spatial coordinates (ξ, η) and (b) 2D contour of the same normalized density field at normalized time $\tau = 0.74$.

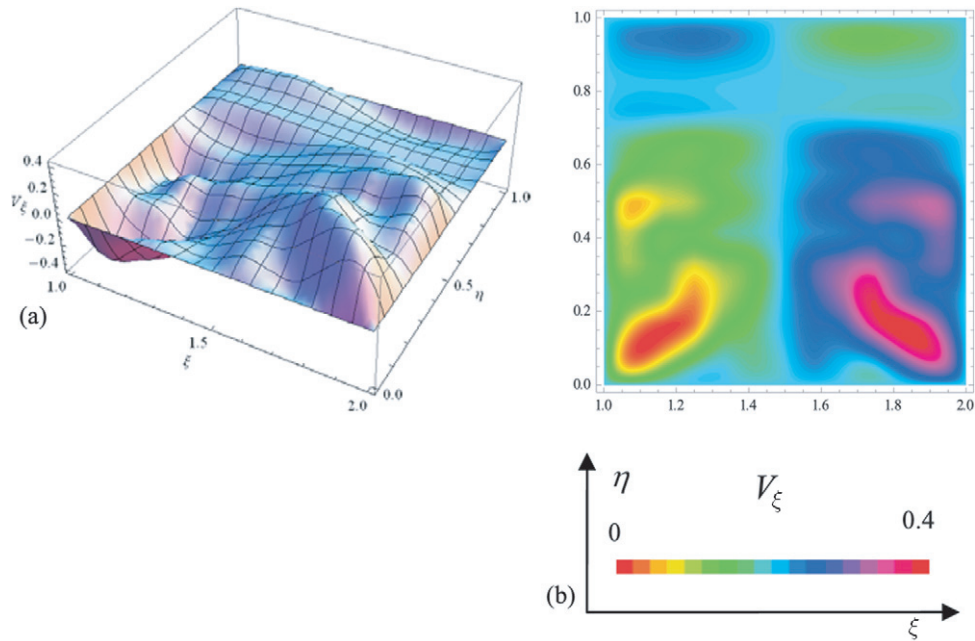


Figure 9. (a) 3D dependence of the normalized speed field V_ξ on the normalized spatial coordinates (ξ, η) and (b) 2D contour of the same normalized speed field at normalized time $\tau = 0.74$.

- symmetry of the normalized speed field V_ξ with respect to the symmetry axis of the spatio-temporal Gaussian (figures 9(a) and (b));
 - shock waves and vortices at the structure’s periphery for the normalized speed field V_η (figures 10(a) and (b));
 - good agreement between the experimental curves in figures 6(a) and (b) and the theoretical ones in figures 11(a) and (b).
- (iv) Chaoticity through non-differentiability (fractalization). In fact, by substituting (10) into (8) and using the method

described in [31–34], the following is obtained:

$$\frac{d\hat{V}}{dt} = -2iD(dt)^{(2/D_F)-1}\nabla \times \left(\frac{\partial \ln \psi}{\partial t} - 2iD(dt)^{(2/D_F)-1} \frac{\nabla \psi}{\psi} \right) = 0. \quad (24)$$

Equation (24) can be integrated in a universal way and yields

$$\hat{L}\psi = 0, \quad (25)$$

$$\hat{L} = 4D^2(dt)^{(4/D_F)-2}\Delta + 2iD(dt)^{(2/D_F)-1} \frac{\partial}{\partial t}, \quad (26)$$

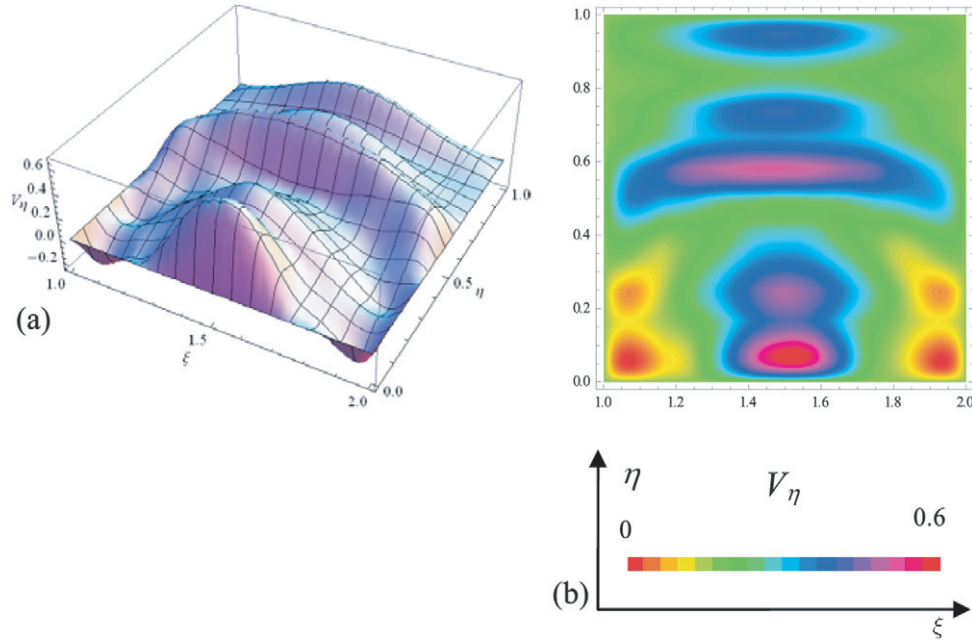


Figure 10. (a) 3D dependence of the normalized speed field V_η on the normalized spatial coordinates (ξ, η) and (b) 2D contour of the same normalized speed field at normalized time $\tau = 0.74$.

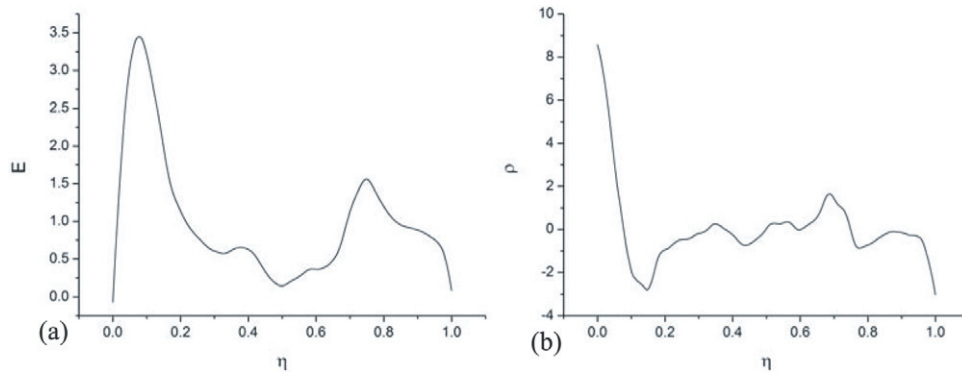


Figure 11. Profile of (a) the normalized electric field and (b) charge density for $\xi = 0.3$.

up to an arbitrary phase factor, which may be set to zero by a suitable choice of the phase of ψ . Equation (25), where \hat{L} is the differential operator (26), is of Schrödinger type. If the discharge plasma is placed in the external field U , then (25) and (26) become

$$\hat{L}_1 \psi = 0, \quad (27)$$

$$\hat{L}_1 = 4D^2(dt)^{(4/D_F)-2} \Delta + 2iD(dt)^{(2/D_F)-1} \frac{\partial}{\partial t} - U. \quad (28)$$

Since the position vector of the particle is assimilated with a stochastic process of Wiener type (for details see [17, 27]), ψ is not only the scalar potential of a complex speed (through $\ln \psi$), but also the density of probability (through $|\psi|^2$) in the frame of a Schrödinger-type theory. It results in the equivalence between the fractal hydrodynamics—see (14)–(16)—and the Schrödinger-type equation—see (25) and (26)—as well as the chaoticity through stochasticization via fractalization. Now, by considering that the potential applied on the electrode immersed into the plasma simulates, in our opinion, an infinite

one-dimensional (1D) potential well, according to the method described in [34], we obtain the discrete energy eigenvalues after solving either the time-independent fractal hydrodynamic equations (14)–(16), or the time-independent Schrödinger-type equation (27):

$$E_n \equiv Q_n = 2m_0 D^2 (dt)^{(4/D_F)-2} \left(\frac{n\pi x}{a} \right)^2, \quad n = 1, 2, \dots \quad (29)$$

and the eigenfunctions

$$\Phi_n = \left(\frac{2}{a} \right)^{1/2} \sin \frac{n\pi x}{a}, \quad (30)$$

where a is the well's width and m_0 is the mass of the fluid particle.

Let us consider the expression $k_n^2 = n^2 k_1^2$ induced by the generalized coherence (in the present context, the physical meaning of the generalized coherence refers to the generation of multiple double layers; for details see [38, 39]). Then, the relation

$$Q_n = Q_1 n^2 \quad (31a)$$

with

$$Q_1 = 2m_0 D^2 k_1^2, \quad k_1 = \frac{\pi}{a}, \quad D = D(dt)^{(2/D_F)-1} \quad (31b-d)$$

expanded around \bar{n} either in the form

$$Q_n = Q_1 \bar{n}^2 + 2Q_1 \bar{n}(n - \bar{n}) + Q_1(n - \bar{n})^2 \quad (32)$$

or in the form

$$Q_n = Q_{\bar{n}} + 4\pi m_0 D \left[\frac{(n - \bar{n})}{T_\alpha} + \frac{(n - \bar{n})^2}{T_\beta} \right], \quad (33a,b)$$

$$Q_{\bar{n}} = Q_1 \bar{n}^2$$

gives the characteristic times:

$$T_\alpha = \frac{2\pi m_0 D}{\bar{n} Q_1}, \quad (34a,b)$$

$$T_\beta = \frac{4\pi m_0 D}{Q_1}.$$

Because T_β is independent of \bar{n} , expression (34b) defines a universal time scale. By means of relations (34b) and (31b), a characteristic frequency can be obtained:

$$f_0 = \frac{1}{T_\beta} = \frac{k_1}{2\pi} \left(\frac{Q_1}{2m_0} \right)^{1/2}. \quad (35)$$

Let us evaluate expression (35) with respect to our experimental results. Thus, by identifying a with a characteristic length of the double layer, namely its width (see also [40–42]), $a = (2\epsilon_0 V/en_0)^{1/2}$, expression (35) takes the form

$$f_0 = \frac{1}{2} \left(\frac{en_0 Q_1}{m_0 \epsilon_0 V} \right)^{1/2}, \quad (36)$$

where Q_1 is the ion energy, m_0 is the ion mass, n_0 is the ion density in the double layer and V is the voltage on the double layer. For our experimental conditions $kT_i \simeq 0.2$ eV, $n_e \simeq n_i = n_0 \simeq 10^9$ cm⁻³, $m_i = m_0 \simeq 40$ amu and $V \simeq 100$ V, we obtain the width of the double layer $a \simeq 3.3$ mm and the disruption frequency $f_0 \simeq 150$ kHz. These values are in good agreement with those experimentally obtained by us (see figure 5) as well as with those from the literature [20, 32, 43].

Now, the fractional revival formalism may be applied. Fractional revival of a physical function occurs when a physical function evolves in time to a state that can be described as a collection of spatially distributed physical sub-functions each of which closely reproduces the initial physical function shape; see [44] for details. In this context, we write the particle's initial ($t = 0$) scalar potential speed function in the square well as

$$\psi(x, t = 0) = \psi_i(x). \quad (37)$$

We expand this scalar potential speed function using relation (30):

$$\psi_i(x) = \sum_{n=1}^{\infty} c_n \phi_n(x) \quad (38)$$

with

$$c_n = \int_{-\infty}^{+\infty} \phi_n(x) \psi_i(x) dx. \quad (39)$$

Using the time scale T_β , the time evolution of the system is found from the Schrödinger-type equation (28) to be

$$\psi(x, t) = \sum_n \exp[-i2\pi(t/T_\beta)n^2] c_n \psi_n(x). \quad (40)$$

A function $F(n)$, whose domain is restricted to the integers ($n \in \mathbb{Z}$), can be written as a finite sum of exponentials if and only if it is r -periodic, that is, if there is an integer r such that $F(n) = F(n+r)$ for all n . Such a finite sum is called *the finite Fourier series* (see also [45]).

In our case, we identify $F(n) = \exp[-i2\pi(t/T_\beta)n^2]$. The necessary and sufficient condition for this exponential to be a periodic function of the quantum number n is that the time ratio t/T_β must be rational, and we write

$$T(p, q) = \frac{p}{q} T_\beta \quad (41)$$

for relatively prime integers p and q (that is, p/q forms a simplified fraction). In terms of frequency, expression (41) takes the form

$$f(p, q) = \frac{1}{T(p, q)} = \frac{q}{p} f_0, \quad f_0 = \frac{1}{T_\beta}. \quad (42a,b)$$

The condition $p > q$ specifies the presence of sub-harmonics in the Fourier spectra.

Now, through the fractal expressions

$$E_1 = \frac{m_0 V^2}{2} = 4\pi m_0 D \frac{p}{q} f(p, q) \quad (43)$$

we can introduce the Reynolds's 'fractional' criterion [46]

$$\text{Re}(p, q) = \frac{V_c L_c}{\tilde{v}} = \frac{p}{q}, \quad (44)$$

where we used the following substitutions:

$$V_c = V, \quad L_c = V f^{-1}(p, q), \quad \tilde{v} = 8\pi D(dt)^{(2/D_F)-1}. \quad (45a-c)$$

From (42) and [46] it results in a critical value for the Reynolds number, Re_c . Up to this value the fractal fluid flow becomes turbulent. Because from (42a) with $p > q$ it results in sub-harmonics for Re_c , according to [47–49], a criterion of evolution to chaos through a cascade of spatio-temporal sub-harmonic bifurcations is stated. We call this criterion the 'fractional' criterion of transition to chaos.

4. Conclusion

A scenario of transition to chaos through a cascade of sub-harmonic bifurcations was experimentally evidenced in connection to the generation and dynamics of concentric multiple double layers in a discharge plasma.

Non-linear dynamics analyses were performed at different increasing values of the voltage applied to the electrode.

Moreover, the axial profiles of the electric field and respectively charge density in front of the electrode were plotted.

By considering that the particle movements in a dc gas discharge plasma take place on fractal curves, a mathematical model according to SRT was developed in order to describe the dynamics of a discharge plasma. Thus,

- (i) using the fractal hydrodynamics, self-structuring of a discharge plasma as concentric multiple double layer was analyzed. In this conjecture, good similarity between the experimental and theoretical dependences was obtained;
- (ii) using the fractional revival formalism, a Reynolds's fractional criterion of evolution to chaos through a cascade of spatio-temporal sub-harmonic bifurcations was stated.

As a final conclusion, one can observe the good agreement between the experimental results and those theoretically obtained.

Acknowledgment

The work was supported by a grant of the Romanian National Authority for Scientific Research, CNCS-UEFISCDI, project number PN-II-ID-PCE-2011-3-0650.

Appendix

The fractal potential Q can generate a viscosity stress type tensor. In fact, written in the form

$$\bar{Q} = -m_0 D^2 (dt)^{(4/D_F)-2} \left[\frac{\nabla^2 \rho}{\rho} - \frac{1}{2} \left(\frac{\nabla \rho}{\rho} \right)^2 \right] \quad (\text{A.1})$$

the fractal potential induces the symmetric tensor

$$\begin{aligned} \sigma_{il} &= m_0 D^2 (dt)^{(4/D_F)-2} \rho \nabla_i \nabla_l \ln \rho \\ &= m_0 D^2 (dt)^{(4/D_F)-2} \left[\nabla_i \nabla_l \rho - \frac{(\nabla_i \rho)(\nabla_l \rho)}{\rho} \right]. \end{aligned} \quad (\text{A.2})$$

The divergence of this tensor is equal to the force density associated with \bar{Q} :

$$\nabla \cdot \bar{\sigma} = -\rho \nabla \bar{Q}. \quad (\text{A.3})$$

The quantity $\bar{\sigma}$ can be identified with the tensor of viscosity stress in a Navier–Stokes-type equation:

$$m_0 \rho \frac{d\mathbf{V}_D}{dt} = \nabla \cdot \bar{\sigma}. \quad (\text{A.4})$$

The momentum flux density type tensor is

$$\pi_{il} = m_0 \rho V_{Di} V_{Dl} - \sigma_{il}, \quad (\text{A.5})$$

and it satisfies the momentum flow type equation

$$m_0 \frac{\partial}{\partial t} (\rho \mathbf{V}_D) = -\nabla \cdot \bar{\pi}. \quad (\text{A.6})$$

In order to complete the analogy with classical fluid mechanics, we formally introduce the kinematical and dynamical types' viscosities:

$$\nu = \frac{1}{2} D (dt)^{(2/D_F)-1}, \quad (\text{A.7})$$

$$\bar{\nu} = \frac{1}{2} m_0 \rho D (dt)^{(2/D_F)-1}. \quad (\text{A.8})$$

The quantities ν and $\bar{\nu}$ are formal viscosities, both of them being induced by the fractal scale. Then, the tensor σ_{il} takes the usual form

$$\sigma_{il} = \bar{\nu} \left(\frac{\partial V_{Fi}}{\partial x_l} + \frac{\partial V_{Fl}}{\partial x_i} \right). \quad (\text{A.9})$$

In particular, if σ_{il} is diagonal,

$$\sigma_{il} = \sigma \delta_{il}, \quad (\text{A.10})$$

equations (14) and (15) in this paper take the form

$$m_0 \left[\frac{\partial \mathbf{V}_D}{\partial t} + (\mathbf{V}_D \cdot \nabla \mathbf{V}_D) \right] = -\frac{\nabla \sigma}{\rho}, \quad (\text{A.11})$$

$$\frac{\partial \rho}{\partial t} + \nabla \cdot (\rho \mathbf{V}_D) = 0. \quad (\text{A.12})$$

Let us now consider that the movements of the plasma particles take place on Peano-type curves (for details see [17, 27–30]). Then, if we assimilate the tensor (A.9) with the gas pressure, i.e. $\sigma_{il} = p \delta_{il}$, equations (A.11) and (A.12) are reduced to the classical plasma hydrodynamics.

References

- [1] Chan C and Hershkowitz N 1982 Transition from single to multiple double layers *Phys. Fluids* **25** 2135–7
- [2] Intrator T, Menard J and Hershkowitz N 1993 Multiple magnetized double layers in the laboratory *Phys. Fluids B* **5** 806–11
- [3] Conde L and León L 1994 Multiple double layers in a glow discharge *Phys. Plasmas* **1** 2441–7
- [4] Nerushev O A, Novopashin S A, Radchenko V V and Sukhinin G I 1998 Spherical stratification of a glow discharge *Phys. Rev. E* **58** 4897–902
- [5] Strat M, Strat G and Gurlui S 2003 Ordered plasma structures in the interspace of two independently working discharges *Phys. Plasmas* **10** 3592–600
- [6] Novopashin S A, Radchenko V V and Sakhapov S Z 2008 Three-dimensional striations of a glow discharge *IEEE Trans. Plasma Sci.* **36** 998–9
- [7] Ionita C, Dimitriu D G and Schrittwieser R W 2004 Elementary processes at the origin of the generation and dynamics of multiple double layers in DP machine plasma *Int. J. Mass Spectrom.* **233** 343–54
- [8] Aflori M, Amarandei G, Ivan L M, Dimitriu D G and Sanduloviciu M 2005 Experimental observation of multiple double layers structures in plasma: I. Concentric multiple double layers *IEEE Trans. Plasma Sci.* **33** 542–3
- [9] Ivan L M, Amarandei G, Aflori M, Mihai-Plugaru M, Dimitriu D G, Ionita C and Schrittwieser R W 2005 Physical processes at the origin of the appearance and dynamics of multiple double layers *Acta Phys. Slovaca* **55** 501–6
- [10] Dimitriu D G, Aflori M, Ivan L M, Ionita C and Schrittwieser R W 2007 Common physical mechanism for concentric and non-concentric multiple double layers in plasma *Plasma Phys. Control. Fusion* **49** 237–48
- [11] Chiriac S, Aflori M and Dimitriu D G 2006 Investigation of the bistable behaviour of multiple anodic structures in dc discharge plasma *J. Optoelectron. Adv. Mater.* **8** 135–8
- [12] Sanduloviciu M and Lozneau E 1986 On the generation mechanism and the instability properties of anode double layers *Plasma Phys. Control. Fusion* **28** 585–95
- [13] Conde L, Ferro Fontán C and Lambás J 2006 The transition from an ionizing electron collecting plasma sheath into an anodic double layer as a bifurcation *Phys. Plasmas* **13** 113504

- [14] Popescu S 2006 Turing structures in dc gas discharges *Europhys. Lett.* **73** 190–6
- [15] Lichtenberg A J and Leiberman M A 1983 *Regular and Stochastic Motion* (New York: Springer)
- [16] Nottale L 1989 Fractals and the quantum theory of spacetime *Int. J. Mod. Phys. A* **4** 5047–117
- [17] Nottale L 1993 *Fractal Space-Time and Microphysics: Towards a Theory of Scale Relativity* (Singapore: World Scientific)
- [18] Feynman R P and Hibbs A R 1965 *Quantum Mechanics and Path Integrals* (New York: McGraw-Hill)
- [19] Dimitriu D G 2004 Physical processes related to the onset of low-frequency instabilities in magnetized plasmas *Czech. J. Phys.* **54** C468–74
- [20] Stenzel R L, Ionita C and Schrittwieser R 2008 Dynamics of fireballs *Plasma Sources Sci. Technol.* **17** 035006
- [21] Stenzel R L, Gruenwald J, Fonda B, Ionita C and Schrittwieser R 2011 Transit time instabilities in an inverted fireball: I. Basic properties *Phys. Plasmas* **18** 012104
- Stenzel R L, Gruenwald J, Fonda B, Ionita C and Schrittwieser R 2011 Transit time instabilities in an inverted fireball: II. Mode jumping and nonlinearities *Phys. Plasmas* **18** 012105
- [22] Stenzel R L, Gruenwald J, Ionita C and Schrittwieser R 2011 Electron-rich sheath dynamics: I. Transient currents and sheath-plasma instabilities *Phys. Plasmas* **18** 062112
- Stenzel R L, Gruenwald J, Ionita C and Schrittwieser R 2011 Electron-rich sheath dynamics: II. Sheath ionization and relaxation instability *Phys. Plasmas* **18** 062113
- [23] Stenzel R L, Gruenwald J, Ionita C and Schrittwieser R 2011 Pulsating fireballs with high-frequency sheath-plasma instabilities *Plasma Sources Sci. Technol.* **20** 045017
- [24] Dimitriu D G, Ignatescu V, Ionita C, Lozneau E, Sanduloviciu M and Schrittwieser R W 2003 The influence of electron impact ionizations on low frequency instabilities in magnetized plasma *Int. J. Mass Spectrom.* **223–224** 141–58
- [25] Chiriac S, Dimitriu D G and Sanduloviciu M 2007 Type I intermittency related to the spatiotemporal dynamics of double layers and ion-acoustic instabilities in plasma *Phys. Plasmas* **14** 072309
- [26] Feigenbaum M J 1980 Universal behavior in nonlinear systems *Los Alamos Sci.* **1** 4–27
- [27] Nottale L 2011 *Scale Relativity and Fractal Space-Time: A New Approach to Unifying Relativity and Quantum Mechanics* (London: Imperial College Press)
- [28] Mandelbrot B 1982 *The Fractal Geometry of the Nature* (San Francisco: Freeman)
- [29] Mandelbrot B 1999 *Multifractals and 1/f Noise* (New York: Springer)
- [30] Agop M, Nica P, Niculescu O and Dimitriu D G 2012 Experimental and theoretical investigations of the negative differential resistance in a discharge plasma *J. Phys. Soc. Japan* **81** 064502
- [31] Agop M, Niculescu O, Timofte A, Bibire L, Ghenadi A S, Nicuta A, Nejneru C and Muncelleanu G V 2010 Non-differentiable mechanical model and its implications *Int. J. Theor. Phys.* **49** 1489–506
- [32] Gurlui S, Agop M, Strat M, Strat G, Bacaita S and Cerepaniuc A 2006 Some experimental and theoretical results on the anodic patterns in plasma discharge *Phys. Plasmas* **13** 063503
- [33] Niculescu O, Dimitriu D G, Paun V P, Matasaru P D, Scurtu D and Agop M 2010 Experimental and theoretical investigations of a plasma fireball dynamics *Phys. Plasmas* **17** 042305
- [34] Agop M, Muncelleanu G V, Niculescu O and Dandu-Bibire T 2010 Static and free time-dependent fractal systems through an extended hydrodynamic model of the scale relativity theory *Phys. Scr.* **82** 015010
- [35] Piel A 2010 *Plasma Physics: An Introduction to Laboratory, Space, and Fusion Plasma* (Berlin: Springer)
- [36] Morozov A I 2012 *Introduction to Plasma Dynamics* (Boca Raton, FL: CRC Press)
- [37] Zienkiewicz O C and Taylor R L 1991 *The Finite Element Method* 4th edn, vol 2 (London: McGraw-Hill)
- [38] Stoler D 1971 Equivalence classes of minimum-uncertainty packets: II *Phys. Rev. D* **4** 1925–6
- [39] Agop M and Mazilu N 1989 *Fundamentals of Modern Physics*: (Iasi: Junimea Publishing House)
- [40] Doggett B and Lunney J G 2009 Langmuir probe characterization of laser ablation plasmas *J. Appl. Phys.* **105** 033306
- [41] Hershkowitz N 2005 Sheaths: more complicated than you think *Phys. Plasmas* **12** 055502
- [42] Charles C 2007 A review of recent laboratory double layer experiments *Plasma Sources Sci. Technol.* **16** R1–25
- [43] Pohoata V, Popa G, Schrittwieser R, Ionita C and Čerček M 2003 Properties and control of anode double layer oscillations and related phenomena *Phys. Rev. E* **68** 016405
- [44] Aronstein D L and Stroud C R 1997 Fractional wave-function revivals in the infinite square well *Phys. Rev. A* **55** 4526–37
- [45] Apostol T M 1976 *Introduction to Analytic Number Theory* (New York: Springer)
- [46] Landau L D and Lifshitz E M 1987 *Fluid Mechanics* 2nd edn (Oxford: Butterworth-Heinemann)
- [47] Arecchi F T, Meucci R, Puccioni G and Tredicce J 1982 Experimental evidence of subharmonic bifurcations, multistability, and turbulence in a Q-switched gas laser *Phys. Rev. Lett.* **49** 1217–20
- [48] Dubois M, Rubio M A and Berge P 1983 Experimental evidence of intermitencies associated with a subharmonic bifurcation *Phys. Rev. Lett.* **51** 1446–9
- [49] Atipo A, Bonhomme G and Pierre T 2002 Ionization waves: from stability to chaos and turbulence *Eur. Phys. J. D* **19** 79–87